RESEARCH ARTICLE SUMMARY

GENE THERAPY

Nonviral delivery of chemically modified tRNA rescues nonsense mutations in cystic fibrosis

Jingan Chen†, Muye Zhou†, Songtao Dong†, Fanglin Gong, Rasangi Tennakoon, Breanna Y. Seto, Ziyan Rachel Chen, Zhichang Peter Zhou, Jingyi Pan, Yue Xu, Sijin Luozhong, Colette Maya Macarios, Santiago Tijaro-Bulla, Tanja Gonska, Jim Hu, Haissi Cui*, Bowen Li*

Full article and list of author affiliations: https://doi.org/10.1126/science.aeb0054

INTRODUCTION: Nonsense mutations introduce premature termination codons (PTCs) into messenger RNAs (mRNAs), preventing full-length protein production and accounting for ~11% of human genetic diseases. Current therapeutic strategies remain limited: Gene-editing approaches can face challenges related to delivery, immunogenicity, and off-target effects, whereas pharmacological readthrough agents have shown limited efficacy or considerable toxicity. Suppressor transfer RNAs (sup-tRNAs), whose anticodons are engineered to read through PTCs, offer an RNA-level strategy for restoring endogenous protein synthesis without altering the genome. This reversibility, transcript-level action, limited detectable off-target activity, and potential applicability across diseases sharing the same nonsense codon make sup-tRNAs attractive therapeutic candidates. However, their therapeutic translation has been limited by suboptimal readthrough, immune activation, short functional persistence, and inefficient delivery to disease-relevant tissues.

RATIONALE: RNA modifications have emerged as key regulators of RNA stability, translation, immunogenicity, and therapeutic performance. Mature endogenous tRNAs are extensively modified for shaping tRNA folding, stability, aminoacylation, decoding, and interactions with the translational machinery. We thus hypothesized that installing defined chemical modifications into engineered sup-tRNAs could improve their activity and suitability as medicines. In parallel, effective translation of tRNA therapeutics requires cargo-tailored delivery vehicles capable of efficiently transporting structured tRNA molecules to disease-relevant tissues. We combined site-specific tRNA engineering with a large lipid nanoparticle (LNP) screen to develop a nonviral delivery platform optimized for sup-tRNA cargo. We used cystic fibrosis (CF) as a disease model to evaluate the therapeutic efficacy of this sup-tRNA platform because nonsense mutations in the cystic fibrosis transmembrane conductance regulator (CFTR) gene represent an unmet clinical need.

RESULTS: We synthesized various chemically modified sup-tRNAs and systematically tested the effects of site-specific modifications. Incorporation of N^1-methyladenosine (m^1A) at position 57 or 58 improved sup-tRNA function, increasing PTC readthrough by up to 10.6-fold for an arginine sup-tRNA. This modification also improved aminoacylation, increased functional persistence, reduced innate immune activation, and benefited sup-tRNAs charged with different amino acids. Screening more than 1000 ionizable lipids identified TTP-3 (tRNA-tailored pulmonary delivery–3), an LNP optimized for sup-tRNA cargo. After intratracheal administration in mice, TTP-3 LNPs efficiently delivered sup-tRNAs to airway epithelial and progenitor cells and showed preliminary aerosolization compatibility. Mango II aptamer insertion enabled in vivo tracking of sup-tRNA biodistribution, revealing delivery to epithelial progenitor cells relevant to CFTR expression and airway repair. In CFTR-mutant bronchial epithelial cells, modified sup-tRNAs restored CFTR protein expression and channel activity. In a CFTR R553X mouse model, LNP–sup-tRNA treatment improved CFTR-dependent swelling in intestinal organoids. In a CF patient–derived organoid model carrying a complex CFTR genotype, cotreatment with sup-tRNAs and Trikafta restored CFTR function, consistent with complementary restoration of protein production and modulator-responsive CFTR activity.

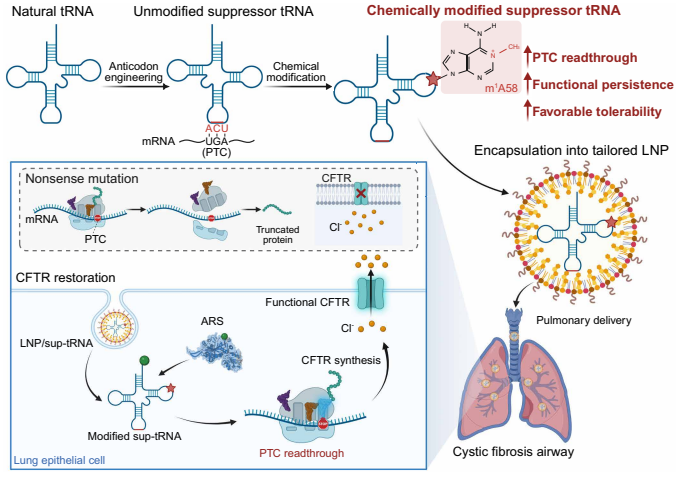

LNP delivery of chemically modified sup-tRNAs for pulmonary nonsense-mutation rescue. Sup-tRNAs decode PTCs to overcome nonsense mutations. Chemical RNA modifications improved sup-tRNA therapy efficacy by enhancing PTC readthrough and functional persistence while reducing immune activation. A tailored LNP delivered modified sup-tRNAs to airway epithelial cells after intratracheal administration, restoring full-length CFTR production and chloride-channel function. ARS, aminoacyl-tRNA synthetase. [Figure created with BioRender.com]

CONCLUSION: This work establishes a chemically modified, nonvirally delivered sup-tRNA platform for rescuing disease-causing nonsense mutations. Site-specific $m^1A57/58$ modification provides a chemical strategy for enhancing sup-tRNA activity, persistence, and tolerability, whereas TTP-3 LNPs illustrate the importance of cargo-specific delivery design for structured tRNA therapeutics. The aptamer-tagging approach further provides a general method for tracking tRNA biodistribution and cell type targeting in vivo. These findings provide broadly applicable engineering insights for the future development of tRNA-based medicines. □

*Corresponding author. Email: bw.li@utoronto.ca (B.L.); haissi.cui@utoronto.ca (H.C.)
†These authors contributed equally to this work. Cite this article as J. Chen *et al.*, *Science* **393**, eaeb0054 (2026). DOI: 10.1126/science.aeb0054

GENE THERAPY

Nonviral delivery of chemically modified tRNA rescues nonsense mutations in cystic fibrosis

Jingan Chen[1,2]†, Muye Zhou[1]†, Songtao Dong[1]†, Fanglin Gong[1,2], Rasangi Tennakoon[3], Breanna Y. Seto[1,3], Ziyan Rachel Chen[4,5], Zhichang Peter Zhou[4], Jingyi Pan[4], Yue Xu[1], Sijin Luozhong[1], Colette Maya Macarios[3], Santiago Tijaro-Bulla[3], Tanja Gonska[4,6], Jim Hu[4,5], Haissi Cui[3]*, Bowen Li[1,2,3,7]*

Suppressor transfer RNAs (sup-tRNAs) can rescue disease-causing nonsense mutations by promoting readthrough of premature termination codons (PTCs). Their clinical translation is limited by suboptimal activity and inefficient in vivo delivery. In this work, we combined site-specific chemical modification of sup-tRNAs with cargo-tailored pulmonary lipid nanoparticle (LNP) engineering to overcome these barriers. Incorporation of N^1-methyladenosine in sup-tRNAs improved PTC readthrough, enhanced tRNA aminoacylation, prolonged functional persistence, and reduced innate immune activation. High-throughput ionizable lipid screening and formulation optimization identified a sup-tRNA–tailored LNP that efficiently delivered chemically modified sup-tRNAs to the lung. This approach restored cystic fibrosis transmembrane conductance regulator (CFTR) expression and function in bronchial epithelial cells, mouse models, and patient-derived organoids. Thus, LNP-delivered, chemically engineered sup-tRNAs represent a potential therapeutic platform for treating nonsense mutations.

Nonsense mutations introduce premature termination codons (PTCs) into mRNAs, prematurely terminating mRNA translation and producing truncated, nonfunctional proteins. These mutations mostly arise from single-nucleotide substitutions within coding regions and account for ~11% of human genetic disorders, typically causing loss-of-function phenotypes (*1*–*3*). Pharmacological readthrough agents generally exhibit limited efficacy and dose-limiting toxicity, whereas gene-replacement and genome-editing strategies require careful evaluation of immunogenicity, off-target effects, and long-term safety (*4*–*6*). Transfer RNAs (tRNAs), which decode mRNA codons by delivering amino acids to the ribosome, have emerged as a broadly applicable therapeutic modality (*7*, *8*). By replacing the anticodon to recognize PTCs, tRNAs can be engineered into suppressor tRNAs (sup-tRNAs), which are aminoacylated by endogenous aminoacyl-tRNA synthetases (ARSs) and restore full-length protein synthesis through translational readthrough (Fig. 1A) (*9*–*11*). Sup-tRNAs can also indirectly stabilize target transcripts by preventing nonsense-mediated decay while minimally perturbing normal translation termination, which makes them a potentially precise and safe strategy for treating nonsense mutations (*12*, *13*).

Previous studies have demonstrated therapeutic rescue of nonsense mutations using either DNA-encoded sup-tRNAs delivered by adeno-associated virus (AAV) or unmodified in vitro transcribed sup-tRNAs delivered by lipid nanoparticles (LNPs) (*14*–*21*). However, clinical translation remains limited by insufficient efficacy and inefficient delivery. Readthrough efficiency depends on the local sequence context, translation velocity, and the identity of the inserted amino acid, and even sequence-optimized sup-tRNAs often fail to achieve therapeutically meaningful rescue (*21*–*26*). Endogenous mature tRNAs contain extensive posttranscriptional nucleoside modifications that regulate folding, stability, decoding, and translational fidelity (Fig. 1B) (*27*–*33*). We hypothesized that introducing defined chemical modifications into therapeutic sup-tRNAs would enhance their stability and readthrough activity.

Efficient in vivo delivery represents a second major barrier to sup-tRNA therapy. Although AAV vectors can provide durable expression, their immunogenicity and limited capacity for redosing restrict clinical utility (*34*, *35*). LNPs offer a clinically validated, nonviral alternative with versatile cargo encapsulation, low immunogenicity, and compatibility with repeated administration (*36*–*38*). However, existing LNP-mediated sup-tRNA delivery has relied on formulations optimized for hepatic mRNA delivery, leaving efficient extrahepatic tRNA delivery largely unexplored. This limitation is particularly relevant to cystic fibrosis (CF), where ~10% of patients harbor nonsense mutations in the cystic fibrosis transmembrane conductance regulator (CFTR) gene and cannot benefit from approved CFTR modulators, such as Trikafta (*39*). In this work, we addressed these challenges by combining site-specific chemical modification of sup-tRNAs with pulmonary LNP engineering.

Select chemical modifications improve sup-tRNA PTC readthrough efficiency and lower immunogenicity

To test the effect of chemical modifications on sup-tRNA, we first studied their impact on Gly–sup-tRNA. We selected GlyTGAchr19trna2 (*14*) as the blueprint for glycyl–sup-tRNA–mediated UGA readthrough because previous sequence-optimization approaches had yielded limited improvement (*21*, *26*). First, we synthesized various chemically modified sup-tRNAs with both naturally occurring and other modifications at distinct structural regions of the tRNA (*40*). Modifications were installed in the D-loop, T-loop, anticodon loop, and acceptor stem (Fig. 1C). D-loop variants included tGM1 [1-methylguanosine at position 9 (m^1G9)], tGM2 [1-methyladenosine (m^1A26)], tGM3 (m^1G9 and m^1A26), and tGM4 (m^1A14). m^1G9 and m^1A26 can occur individually or together in tRNAs (*28*). T-loop variants included tGM5 [5,2′-O-dimethyluridine (m^5Um54)] and tGM6 (m^1A57/58). Typically, T-loop m^1A modification occurs at position 57 or 58 in tRNAs, and because GlyTGAchr19trna2 lacks adenine at position 58, we introduced the m^1A modification at position 57. Anticodon-loop variants included tGM7 [5-methylcytidine (m^5C32)], tGM8 [2′-O-methyladenosine (Am37)], and tGM9 [N6-methyladenosine (m^6A37)]. Inspired by the immunogenicity-reducing effects of pseudouridine (Ψ) in mRNA therapeutics, we also created a variant with Ψ only (tGM10, 100% Ψ). Additionally, we designed another variant (tGM11) incorporating Ψ specifically at position 34 of the anticodon because pseudouridylation of mRNA at the PTCs enhances near-cognate tRNA readthrough (*41*). Finally, we synthesized tGM12 containing m^1A72 near the CCA end.

To evaluate the efficiency of these chemically modified sup-tRNA variants in decoding PTCs, we generated a reporter cell line based on BEAS-2B (lung epithelial) expressing NanoLuc luciferase (NLuc) with a PTC (UGA) (*14*) (Fig. 1D) and transfected sup-tRNAs using Lipofectamine MessengerMAX for readthrough assay. The modifications added to the tRNA in variants tGM1, tGM2, tGM3, and tGM6 successfully improved readthrough efficiency compared with the unmodified counterpart (fig. S1). On the basis of these results, we explored a potential synergistic effect by combining beneficial modifications, which led to the design of tGM13 (m^1G9, m^1A26, and m^1A57) and tGM14 (m^1G9, m^1A26, m^6A37, and m^1A57). We then tested all fourteen variants together at the same dosage level. At 24 hours posttreatment, increased PTC readthrough was observed for tGM1 (2.2-fold), tGM2 (2.1-fold),

[1]Leslie Dan Faculty of Pharmacy, University of Toronto, Toronto, ON, Canada. [2]Institute of Biomedical Engineering, University of Toronto, Toronto, ON, Canada. [3]Department of Chemistry, University of Toronto, Toronto, ON, Canada. [4]Program in Translational Medicine, The Hospital for Sick Children Research Institute, Toronto, ON, Canada. [5]Department of Laboratory Medicine and Pathobiology, University of Toronto, Toronto, ON, Canada. [6]Pediatric Gastroenterology, Department of Pediatrics, University of Toronto, Toronto, ON, Canada. [7]Princess Margaret Cancer Centre, University Health Network, Toronto, ON, Canada.
***Corresponding author. Email: bw.li@utoronto.ca (B.L.); haissi.cui@utoronto.ca (H.C.)**
†These authors contributed equally to this work.

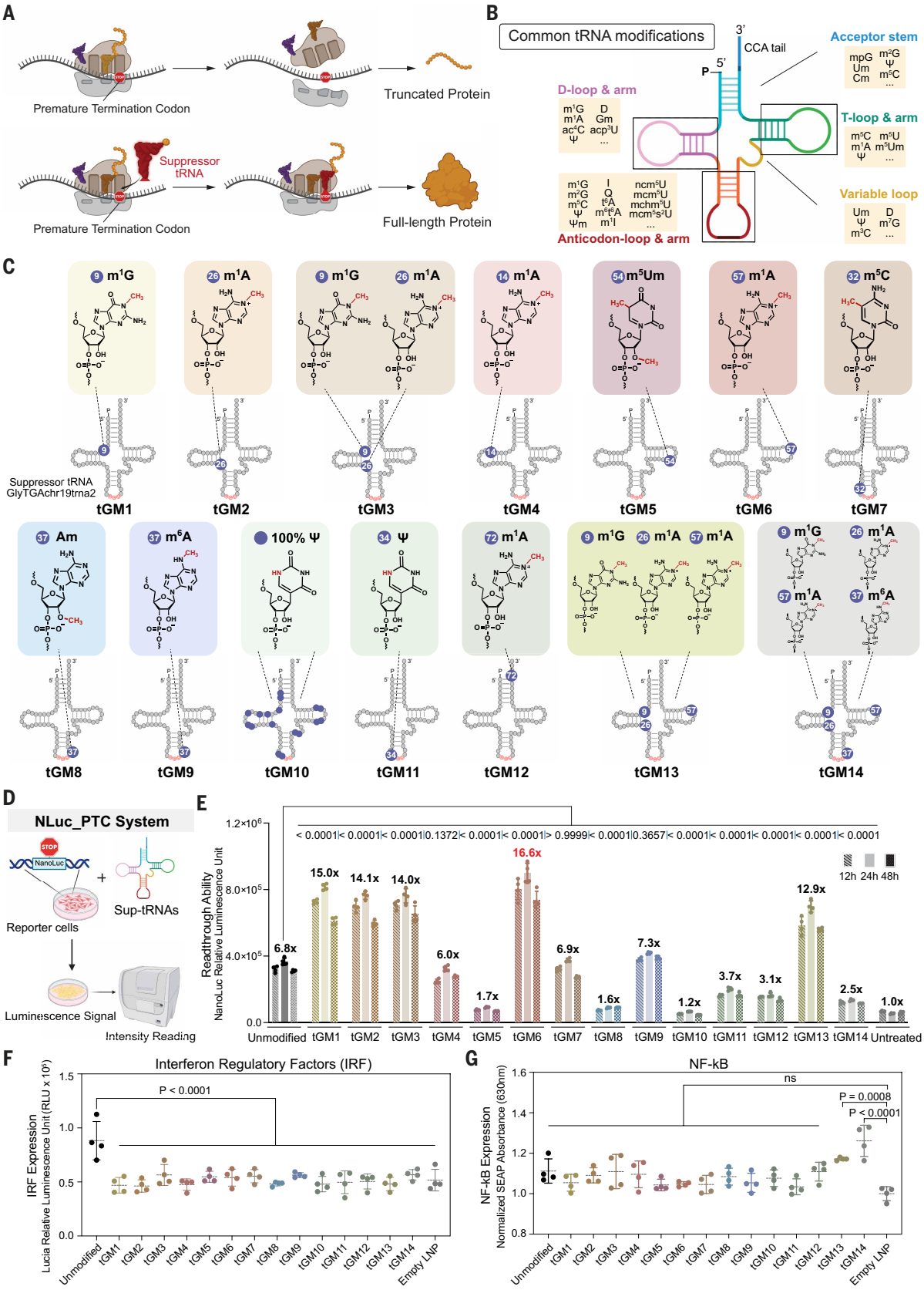

Fig. 1. Effect of RNA chemical modifications on sup-tRNA readthrough efficiency and immunogenicity. (**A**) Illustration of sup-tRNA–mediated readthrough of PTCs to restore full-length protein synthesis. (**B**) Naturally occurring chemical modifications in tRNAs. (**C**) Schematic representation of glycine sup-tRNAs engineered with a 5′-UCA-3′ anticodon to decode the UGA stop codon, incorporating various site-specific RNA modifications (tGM1 to tGM14). (**D**) Scheme of the NanoLuc luciferase (NLuc) with PTC reporter system for evaluating readthrough efficiency of sup-tRNA variants. (**E**) Comparative assessment of sup-tRNA variant readthrough activity in NLuc-PTC reporter at

different time points (12, 24, and 48 hours posttreatment) with the same dosage level (300 ng per 10^5 cells). Readthrough assays were performed after Lipofectamine MessengerMAX-mediated tRNA transfection. Values represent fold changes relative to untreated controls. $n = 4$ independent replicates. (**F** and **G**) Immunogenicity profiling of sup-tRNA variants in THP-1 dual-reporter cells, which monitor the activation of the IRF pathway (F) and NF-κB signaling pathway (G). Sup-tRNA variants were delivered using SM-102 LNPs. Data are means ± SDs; $n = 4$ independent replicates. In (E), *P* values for 24-hour data were calculated by one-way ANOVA with Dunnett's multiple-comparison test versus unmodified sup-tRNA. In (F) and (G), *P* values were calculated by one-way ANOVA with Tukey's multiple-comparison test. ns, not significant.

tGM3 (2.1-fold), tGM6 (2.4-fold), tGM9 (1.1-fold), and tGM13 (1.9-fold) relative to the unmodified sup-tRNA (Fig. 1E). Among these, tGM6 showed the largest improvement (2.4-fold). By contrast, tGM4 (0.9-fold), tGM5 (0.3-fold), tGM8 (0.2-fold), tGM10 (0.2-fold), tGM11 (0.6-fold), tGM12 (0.5-fold), and tGM14 (0.4-fold) reduced readthrough activity, whereas tGM7 produced readthrough levels comparable to the unmodified counterpart. This trend remained consistent across three time points (12, 24, and 48 hours posttreatment). We further evaluated all variants in additional cell lines, including HepG2, C2C12, and THP-1. Although absolute PTC readthrough values differed among cell lines, the relative performance of the variants was largely conserved, which indicates that readthrough efficiency was preserved across cellular contexts (fig. S2).

We next assessed the immunogenicity of the sup-tRNA variants in THP-1 dual-reporter cells (human monocytes), which enable simultaneous monitoring of nuclear factor κB (NF-κB) and interferon regulatory factor (IRF) pathway activation. To distinguish immunogenic effects arising from the delivery vehicle versus the tRNA variants, the library was formulated into LNPs containing either of two ionizable lipids with distinct inflammatory profiles—SM-102 (lower inflammatory potential) or cKK-E12 (higher inflammatory potential)—with the same formulation. At the tRNA dose used in the readthrough assays, delivery by SM-102 LNPs, which cause minimal intrinsic immune activation, showed that the unmodified sup-tRNA activated the IRF pathway, whereas none of the chemically modified variants triggered detectable IRF activation (Fig. 1F). NF-κB signaling was activated only by tGM13 and tGM14, both containing multiple modifications (Fig. 1G). To further characterize these inflammatory responses, we performed dose-response analyses concomitantly with cell-viability measurements. Cell viability remained high across all variants and doses, which indicated that the observed responses were not attributable to cytotoxicity (fig. S3). Similar trends observed across SM-102 and cKK-E12 formulations suggested that the differences primarily reflected varying tRNA modifications rather than LNP-induced immunogenicity. This unintended NF-κB activation may explain the absence of synergistic enhancement in readthrough activity observed for variants combining multiple modifications that were beneficial by themselves. Together, these results highlight the importance of site-specific modifications, especially $m^1A57/58$, in improving PTC readthrough efficiency while maintaining a favorable immunological profile.

m^1A58 modification enhances aminoacylation efficiency and extends PTC readthrough duration

tRNAs are charged with the correct amino acid by ARSs, and the efficiency of this process influences mRNA translation and cellular homeostasis (*42*) (Fig. 2A). Efficient aminoacylation is particularly critical for sup-tRNA therapies as a prerequisite for function. However, changing the anticodon to generate sup-tRNAs can reduce ARS recognition and lower aminoacylation activity toward sup-tRNAs. We thus evaluated the aminoacylation efficiency toward modified Gly–sup-tRNA variants using recombinant human glycyl-tRNA synthetase (GARS1) (*43*). In vitro incubation with GARS1 and subsequent analysis of tRNA charging levels by acid gel (Fig. 2B and fig. S4) showed that 84% of native Gly-tRNA was aminoacylated. In comparison, aminoacylation levels were lowered upon mutation of the anticodon to sup-tRNA (~30%) as expected because the anticodon serves as an identity motif in Gly-tRNA (*44*, *45*). In several sup-tRNA variants, chemical modifications caused substantially increased charging relative to the unmodified sup-tRNA, including tGM1 (~55%), tGM2 (~51%), tGM3 (~68%), tGM6 (~63%), and tGM13 (~57%). Other variants were charged similarly to the unmodified sup-tRNA (tGM7, ~35%; tGM8, ~29%; and tGM9, ~30%), whereas some modifications resulted in reduced tRNA aminoacylation (tGM5, ~13%; tGM10, ~11%; and tGM12, ~16%). Overall, efficiently aminoacylated tRNA variants displayed higher readthrough reporter activity in cell assays, which suggests that tRNA aminoacylation was a limiting factor for sup-tRNA potency. In line with this, tGM10, with 100% U→Ψ substitution, was minimally aminoacylated, which indicated that extensive Ψ modifications severely disrupted ARS recognition and consequently explained the low readthrough rates observed in cells. Notably, tGM13 and tGM14, which each combine multiple modifications, were less efficiently charged compared with single-modified variants. This reduction also matched our observations in cell-based reporter assays, highlighting that combining modifications may inadvertently impair aminoacylation and thereby limit therapeutic efficacy in addition to activating the NF-κB pathway (Fig. 1G). Additionally, we explored the importance of the 5′ monophosphate in sup-tRNAs (*46*). We synthesized an alternative version with a 5′ hydroxyl group of the most effective variant, tGM6, which substantially reduced readthrough capability compared with its 5′ monophosphate counterpart (Fig. 2C). This finding highlights the critical role of the correct 5′ end in preserving the high therapeutic efficiency of sup-tRNAs.

To evaluate whether the beneficial effects of the modification in glycine sup-tRNAs could extend to other sup-tRNAs, we synthesized m^1A58-modified versions of arginine and tryptophan sup-tRNAs. The Arg–sup-tRNA sequence was derived from a previously optimized variant known as tRT6 (*21*). We modified tRT6 with m^1A58 (referred to as tRM6 in our study). Introducing the m^1A58 modification significantly enhanced PTC readthrough efficiency in both Arg– and Trp–sup-tRNAs (Fig. 2D and fig. S5), although the magnitude of enhancement differed between the two scaffolds. Notably, tRM6 exhibited an ~10.6-fold increase in PTC readthrough efficiency. To accurately quantify the effect of the m^1A58 modification on sup-tRNA aminoacylation kinetics, we performed filter binding assays using radiolabeled amino acids. The m^1A58-modified Arg–sup-tRNA variant tRM6 was more efficiently aminoacylated compared with both the native arginine tRNA (tR) and the unmodified Arg–sup-tRNA (tRT6). tRM6 was 2.3-fold more efficiently charged compared with tR and 1.7-fold more compared with tRT6 (Fig. 2, E and F).

We next investigated whether the m^1A58 chemical modification could extend the tRNA half-life and the duration of sup-tRNA–mediated PTC readthrough activity in vitro and in vivo. Reporter cells treated with the modified tRM6 still generated NLuc signal after 30 days, whereas the unmodified tRT6 group showed a rapid decline in signal (Fig. 2G). To directly assess sup-tRNA persistence, we performed tRNA sequencing (tRNA-seq) of CF human bronchial epithelial (HBE) cells after treatment with tRM6 or tRT6. The modified sup-tRNA remained more abundant over time and showed significantly greater retention on day 35 than the unmodified tRNA, with an estimated apparent half-life of ~29 days (tRM6) compared with ~12 days (tRT6) (fig. S6). Additionally, the m^1A58 site in tRM6 remained modified throughout the whole time course, at levels comparable to the modification of endogenous arginine tRNA at position 58. By contrast, the unmodified tRT6 showed only minimal modification, indicating limited endogenous methylation after delivery. tRM6 remained predominantly aminoacylated at later time points, indicating sustained integrity and activity. These results indicate that m^1A58 modification enhanced functional

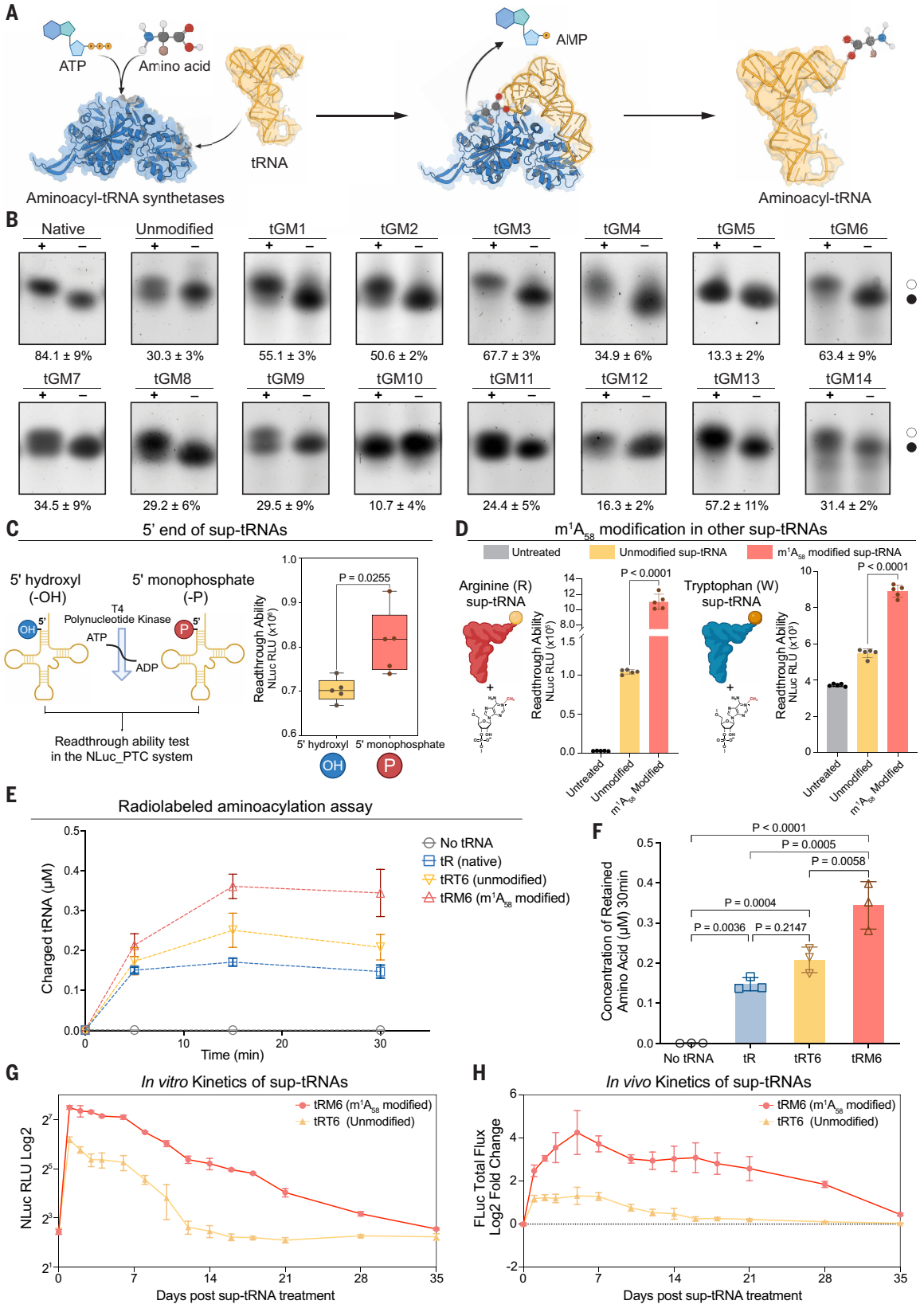

Fig. 2. Characterization of aminoacylation, versatility, and persistence of chemically modified sup-tRNAs. (**A**) Simplified schematic illustrating aminoacylation of tRNAs by ARSs. The structural depiction of glycyl-tRNA synthetase in complex with Gly-tRNA was adapted from PDB ID 4KR2 (RCSB Protein Data Bank). (**B**) Aminoacylation efficiency of Gly-tRNA variants catalyzed by glycyl-tRNA synthetase (GARS1) (+) compared with nonaminoacylated controls (−). Aminoacylated tRNAs (open circles) display slower electrophoretic migration than nonaminoacylated tRNAs (filled circles). $n = 3$ or 4 independent replicates. (**C**) Effect of 5′-hydroxyl (-OH) and 5′-monophosphate (-P) ends on the readthrough efficiency of sup-tRNA assessed by NLuc_PTC reporter. $n = 5$ independent replicates. (**D**) Enhanced readthrough

efficiency after the installation of m^1A58 across different sup-tRNAs (arginine and tryptophan sup-tRNAs; note that separate *y*-axis scales are used). $n = 5$ independent replicates. (**E** and **F**) Aminoacylation kinetics (E) and quantitative comparison of aminoacylation efficiency at 30 min (F) of arginine sup-tRNA variants using radiolabeled amino acids. $n = 3$ independent replicates. (**G** and **H**) Evaluation of functional persistence of unmodified (tRT6) and m^1A58-modified (tRM6) sup-tRNAs measured by NLuc_PTC reporter in vitro in cell culture (G) and in vivo in the liver of a LumA-PTC reporter mouse line (H). $n = 3$ biological replicates. Cell-based readthrough and sup-tRNA persistence assays in (C), (D), and (G) were performed using Lipofectamine MessengerMAX-mediated transfection; in vivo persistence in (H) was assessed after hepatic LNP delivery. Data are means ± SDs. *P* values were calculated by two-tailed unpaired Student's *t* test in (C) and (D) and one-way ANOVA with Tukey's multiple-comparison test in (F).

persistence. We also compared modified sup-tRNA with exogenous NLuc-encoding mRNA. In the NLuc_PTC reporter cell line, delivery of tRM6 produced more sustained reporter luminescence than direct delivery of NLuc-encoding mRNA over the course of 14 days (fig. S7). Consistent with this functional difference, NLuc mRNA abundance decreased to less than 1% of day 1 levels by day 14, indicating superior stability of modified sup-tRNA compared with mRNA. These findings support an advantage of sup-tRNA–based therapy through the prolonged restoration of endogenous protein over mRNA-based gene replacement for treating disorders caused by nonsense mutations.

For in vivo validation, we used a transgenic LumA mouse model containing a firefly luciferase (FLuc) gene with a UGA PTC (R387X) (*47*). After intravenous administration, FLuc luminescence signals in the liver of tRM6-treated mice remained substantially higher than in tRT6-treated animals and lasted beyond 30 days (Fig. 2H), which underscores the persistent efficacy of m^1A58-modified sup-tRNAs in vivo. Repeated dosing further highlighted the advantage of chemical tRNA modification. After administration on days 0, 14, and 28, the modified sup-tRNA group showed a rapid rebound after each dose and maintained comparable peak activity across all three dosing cycles, whereas the unmodified group exhibited progressively weaker responses with each subsequent administration (fig. S8). This divergence suggests that chemical modification improved the durability of redosing, likely by increasing RNA stability and reducing innate immune sensing that could dampen mRNA translation after repeated RNA delivery.

High-throughput screening to develop LNPs for sup-tRNA pulmonary delivery

Next, we opted to develop a delivery system tailored to sup-tRNAs. LNPs typically comprise ionizable lipids, cholesterol, helper lipids, and PEGylated lipids, with ionizable lipids being the key component for determining delivery potency, biocompatibility, and cell specificity (*48*); because of this, the lipids are the most commonly adjusted component. Owing to the limited understanding of lipid structure-activity relationships, we used high-throughput approaches to screen diverse lipids for LNP development (*49*–*51*). To optimize LNPs specifically for pulmonary sup-tRNA delivery, we combined simple building blocks using a Ugi four-component reaction (Ugi-4CR) (*52*, *53*), which enabled rapid, one-pot synthesis of chemically diverse ionizable lipids (Fig. 3A). By systematically combining 10 amine headgroups, 5 aldehyde linkers, 5 carboxylic acid tails, and 4 isocyanide tails (Fig. 3B), we efficiently synthesized a library of 1000 structurally distinct ionizable lipids in a single day using automated robotic synthesis. To determine whether there are specific LNP design considerations to maximize sup-tRNA delivery, we screened the same 1000-member ionizable lipid library in parallel using either sup-tRNA (a small and highly structured RNA) or mRNA (a larger RNA). These 1000 ionizable lipids were used in the same LNP formulation along with helper lipid, cholesterol, and PEGylated lipid to encapsulate either sup-tRNAs or mRNAs (Fig. 3C) for delivery to BEAS-2B cells. The two screens produced markedly different structure-activity maps, and lipid performance across the library showed only a weak correlation between sup-tRNA and mRNA delivery (Fig. 3, D and E, and fig. S9). Thus, the lipid structure requirements for efficient delivery differ substantially between RNA modalities, supporting the need for cargo-specific lipid screening.

In CF patients, a dense mucus barrier impedes delivery to lung epithelial cells. We thus used a CF-relevant air-liquid interface (ALI) culture model, where bronchial epithelial reporter cells are coated with artificial mucus, to realistically evaluate mucus penetration and cellular transfection by LNPs (Fig. 3F). In this ALI model, we further tested the top 10 ionizable lipids identified from our initial screen and ultimately identified the most promising ionizable lipid candidate, hereafter named TTP-3 (tRNA-tailored pulmonary delivery–3) (fig. S10). TTP-3 exhibited superior transfection performance compared with commercial benchmark lipids when tested with identical formulations, including A10-LIN, which was developed for pulmonary mRNA delivery, and the FDA-approved MC3 (Onpattro), designed for small interfering RNA (siRNA) delivery (Fig. 3G). Notably, A10-LIN still performed favorably relative to several top candidates in the secondary screen, although it was less effective than TTP-3. This suggests that mRNA delivery performance was not a reliable predictor of sup-tRNA delivery efficiency, which supports cargo-specific LNP development rather than extrapolation across RNA modalities. To further optimize the formulation of TTP-3 LNPs, we used a design of experiments (DoE) approach (*54*, *55*) to systematically evaluate seven critical parameters known to influence the transfection efficiency of LNPs: (i) ionizable lipid to RNA mass ratio, (ii) ionizable lipid molar ratio, (iii) type of helper lipid, (iv) helper lipid molar ratio, (v) type of sterol lipid, (vi) sterol lipid molar ratio, and (vii) PEGylated lipid molar ratio (Fig. 3H). Various statistically representative LNP formulations were tested in the ALI model coated with mucus, which allowed us to incorporate both epithelial transfection and the airway mucus barrier into the optimization workflow. The optimized LNP formulation was obtained by using a desirability function, defined by the experimentally observed maximized transfection efficiency across conditions. The resulting optimal formulation for pulmonary sup-tRNA delivery consisted of a 13.5:1 ionizable lipid–to–tRNA mass ratio with 60% TTP-3, 10% DOPE, 27.5% β-sitosterol, and 2.5% PEGylated lipid (Fig. 3I). By contrast, parallel DoE optimization of TTP-3 LNPs carrying mRNA converged on a different formulation (fig. S11), which indicates that both ionizable lipid selection and the optimal LNP composition are cargo dependent. In a mucus-filled parallel channel assay, the TTP-3 with optimized LNP formulation showed the highest diffusivity, exceeding both a TTP-3 formulation prepared according to the Onpattro formulation and MC3 under the same benchmark formulation (fig. S12), which supports its suitability for diffusion in airway mucus. This optimized TTP-3 LNP formulation demonstrated superior sup-tRNA pulmonary delivery in vivo through intratracheal administration in the LumA (FLuc R387X) transgenic reporter mouse model, significantly outperforming both A10-LIN and MC3 LNPs (Fig. 3, J and K, and fig. S13).

Adaptation of sup-tRNA delivery through inhalation would be important for clinical translation, particularly with regard to patient acceptability and repeated dosing (*56*–*58*). Hence, we also assessed the feasibility of nebulizing TTP-3 LNPs loaded with sup-tRNA and confirmed that the nebulized formulation retained PTC readthrough capability in the NLuc_PTC reporter cell system, albeit to a lesser degree than preparations that did not undergo nebulization (fig. S14). To protect LNPs during the nebulization process, we considered increasing polyethylene glycol (PEG) content above 2.5 mol %; however, higher PEG levels progressively reduced transfection efficiency. Addition of

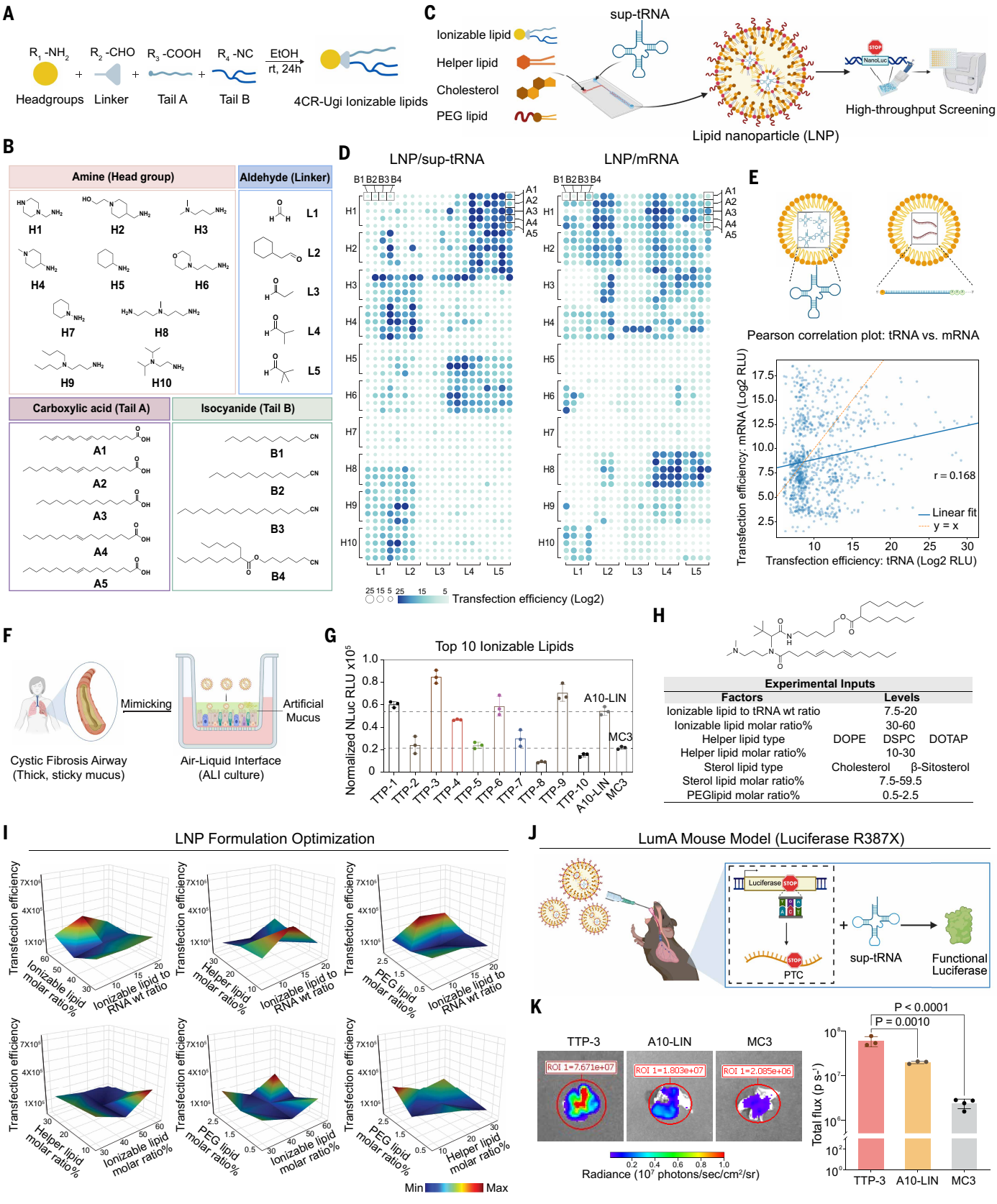

Fig. 3. High-throughput synthesis, screening, and optimization of an ionizable lipid library for sup-tRNA pulmonary delivery. (**A**) Illustration of the Ugi four-component reaction. The library was synthesized from diverse amines (headgroups), aldehydes (linkers), carboxylic acid tails (tail A), and isocyanide tails (tail B). (**B**) Chemical structures of the four components in the synthesis library. (**C**) Schematic depiction of LNP assembly and subsequent high-throughput screening. (**D**) High-throughput screening results of the lipid library. (Top) BEAS-2B reporter cells treated with LNP–sup-tRNA. (Bottom) BEAS-2B cells treated with LNP–FLuc mRNA. Heatmaps show normalized luminescence

intensity (log_2 RLU) representing transfection efficiency. (**E**) Pearson correlation comparing lipid performance for sup-tRNA versus mRNA delivery across the screened library. (**F**) Schematic overview of the ALI culture model incorporating artificial mucus, designed to mimic the viscous mucus characteristic of the CF lung environment. (**G**) Evaluation of the top 10 performing ionizable lipids from the initial screen in CF-mimicking ALI culture. $n = 3$ independent replicates. (**H**) Chemical structure of the best-performing ionizable lipid (TTP-3) and a summary of key experimental parameters for LNP formulation optimization. (**I**) Response surface plots showing desirability function–based optimization of TTP-3 LNP formulation parameters, identifying optimal conditions for sup-tRNA delivery. (**J**) Illustration of the LumA_PTC transgenic mouse model (Fluc R387X), used to assess pulmonary sup-tRNA transfection efficiency by measuring functional luciferase protein restoration. (**K**) Representative IVIS results of lungs obtained at day 3 after intratracheal administration of LNP-tRM6 (1.25 mg/kg) with different ionizable lipids. All LNPs used shared the same formulation optimized from the DoE study (I). $n = 3$ or 4 biological replicates. Data are means ± SDs. *P* values in (K) were calculated by one-way ANOVA with Tukey's multiple-comparison test.

poloxamer 188, which stabilizes LNPs during nebulization (*59*), improved postnebulization encapsulation efficiency and better preserved sup-tRNA activity (fig. S14). These preliminary results support compatibility with aerosolization; however, further optimization of LNP formulation and nebulization conditions could benefit delivery through inhalation. Overall, these findings highlight the importance of a tailored LNP platform to enable effective pulmonary delivery of sup-tRNAs for the treatment of genetic lung disorders.

Fluorescent aptamer–based tracking demonstrates efficient sup-tRNA delivery to lung epithelial and CFTR-resident progenitor cells

To track the biodistribution and cellular targeting efficiency of the optimized LNP for tRNA delivery, we inserted the Mango II fluorogenic aptamer (*60*, *61*) into the variable loop of the sup-tRNA sequence. Upon binding to its fluorophore ligand, the aptamer strongly enhances its fluorescence, which enables direct visualization of tRNA molecules (Fig. 4A). To confirm that aptamer insertion did not compromise sup-tRNA function, we evaluated its performance in NLuc_PTC reporter cells. The Mango II–modified sup-tRNA retained substantial readthrough activity, albeit showing a reduction of ~30 to 40% compared with sup-tRNA alone (fig. S15). Aptamer insertion had no detectable effect on cell viability, LNP encapsulation efficiency, or particle size, which indicated that the modification did not alter key physicochemical properties relevant to delivery and biodistribution. Consequently, the Mango II–modified sup-tRNA (tRNA_Aptamer) was used as a fluorescent tracking probe in subsequent in vivo biodistribution studies.

After intratracheal administration of the LNP-tRNA_Aptamer complex to mice, we analyzed the cellular distribution of the tRNA_Aptamer in the lung using flow cytometry (Fig. 4B and fig. S16). In TTP-3 LNP–treated animals, ~60% of all tRNA_Aptamer-positive cells were epithelial cells, whereas immune and endothelial cells made up ~9% and ~8%, respectively (Fig. 4, C and D). This epithelial-dominant transfection profile is highly beneficial for CF therapy because CFTR mutations primarily affect lung epithelial cells. By contrast, MC3 LNPs (Onpattro) predominantly transfected endothelial cells (~50%) and immune cells (~15%), with substantially fewer positive epithelial cells (~19%). Within the epithelial cell population, ~32% of cells were tRNA_Aptamer positive after treatment with TTP-3 LNP compared with 13% after MC3 LNP treatment (Fig. 4E). We next evaluated the cellular delivery of TTP-3 LNPs to CFTR-relevant airway epithelial populations (fig. S17), including ciliated cells, club cells, ionocytes, and basal stem cells (*56*, *62*). Basal cells are critical target cells for a durable therapeutic benefit owing to their long lifespan and regenerative capacity in the airway epithelium (*63*, *64*). TTP-3 LNPs achieved robust delivery across these populations, targeting 22% of ciliated cells, 19% of club cells, and 32% of basal cells, as shown by tRNA_Aptamer internalization (Fig. 4F). Ionocytes, though rare, exhibited around 15% transfection efficiency—a notable result given their high endogenous CFTR expression (fig. S18). Immunofluorescence staining of lung tissue further confirmed TTP-3 LNP–mediated delivery to these key epithelial and progenitor cells in both the small airways and bronchi (Fig. 4G). Together, these findings established fluorescent aptamer–based tRNA labeling as a generalizable tracking platform for studying the biodistribution and cell type–specific localization of tRNA-based therapeutics.

Therapeutic efficacy of chemically modified sup-tRNAs in CF disease models

We next assessed the therapeutic efficacy of our chemically modified sup-tRNAs in CF disease models. First, we treated 16-HBEge (HBE) cells carrying the CFTR G542X variant with tGM6 (Fig. 5A) but observed only moderate CFTR protein restoration. Given the superior readthrough efficiency of tRM6 in the NLuc_PTC reporter systems (Fig. 2D), we thus tested tRM6 for CFTR restoration in HBE G542X cells. Although tRM6 introduces arginine rather than glycine at the PTC site, previous studies indicated that CFTR G542R remains functional (*17*, *65*). Immunoblot analysis confirmed better CFTR restoration with tRM6 compared with tGM6 (Fig. 5, B and C), highlighting the dependency on high sup-tRNA readthrough efficiency to achieve the desired therapeutic outcome.

Next, we extended our investigation to HBE cells with the R1162X CFTR variant, where tRM6 robustly restored CFTR protein (Fig. 5, D and E, and fig. S19) and maintained substantial CFTR levels beyond 40 days after treatment (fig. S20). Functional validation, using a fluorescence-based assay of membrane potential changes (FLIPR) (*66*, *67*), confirmed enhanced CFTR ion channel activity in tRM6-treated HBE R1162X cells (Fig. 5, F and G). To determine whether sup-tRNA–mediated CFTR expression was accompanied by broader cellular restoration, we performed RNA-seq on sup-tRNA–treated HBE R1162X cells and compared them with untreated R1162X and wild-type (WT) HBE cells. Sup-tRNA treatment increased CFTR transcript abundance to >10% of WT levels (figs. S21 and S22). Treatment-associated gene-expression changes were enriched for processes related to ion transport, extracellular organization, and epithelial homeostasis, partially overlapping with pathways that distinguished WT from untreated mutant cells (Fig. 5, H to J). Thus, sup-tRNA–mediated rescue of CFTR expression and function was associated with a broader shift toward restoring healthy gene expression.

We also examined potential off-target readthrough at canonical stop codons. Ribosome profiling of sup-tRNA–treated HBE R1162X cells showed that ribosome occupancy remained concentrated within coding regions, with low 3′ untranslated region (3′UTR) signal downstream of annotated canonical stop codons and no global increase relative to untreated cells (fig. S23). Minimal off-target readthrough was evident both transcriptome-wide and at the endogenous CFTR transcript. This selectivity likely arose from the distinct sequence context of canonical stop codons and PTCs: Native stop codons reside within a 3′UTR/poly(A)-associated messenger ribonucleoprotein (mRNP) context in which poly(A)-binding protein (PABP) functionally cooperates with eRF1/eRF3–guanosine 5′-triphosphate (GTP) to accelerate termination, allowing release factors to efficiently outcompete sup-tRNAs (*68*). By contrast, PTCs occur within coding regions and are more distant from poly(A)-bounded PABP, which makes them more permissive to sup-tRNA–mediated decoding.

Next, we assessed the pulmonary and systemic safety of intratracheal LNP–sup-tRNA administration in mice. BALF and serum cytokine profiling showed a transient, dose-dependent inflammatory response at day 1, most evident at 5 and 10 mg/kg, whereas 1- and 3-mg/kg–treated groups remained near phosphate-buffered saline (PBS) controls; in all groups, cytokine levels largely returned to baseline by day 14 (fig. S24). Lung histopathology, BALF complement activation,

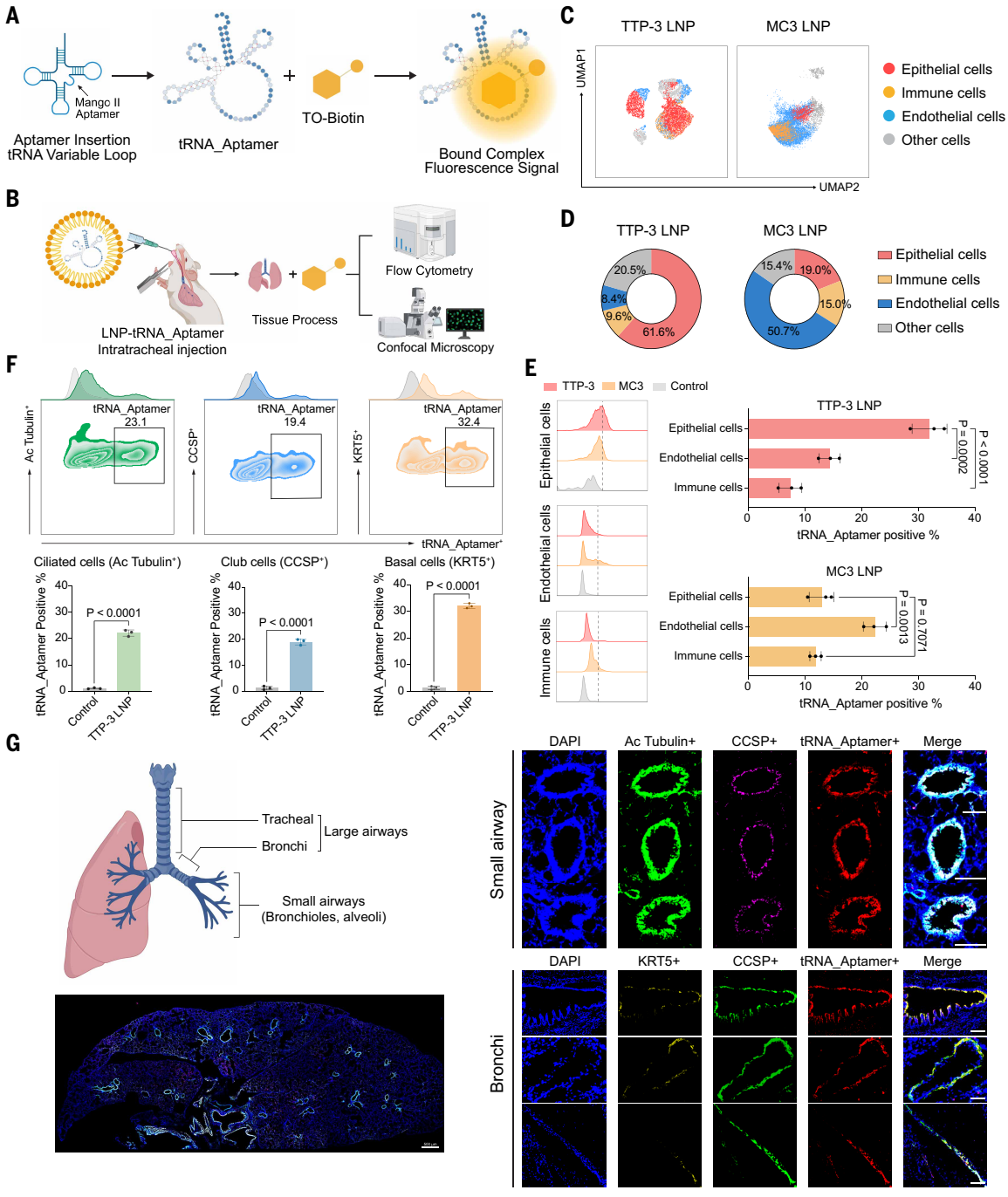

Fig. 4. Aptamer-based visualization reveals epithelial tropism of TTP-3 LNP–delivered sup-tRNAs in vivo. (**A**) Schematic illustration of sup-tRNA modified by fusing a Mango II aptamer to its variable loop. The aptamer specifically binds to thiazole orange (TO)–biotin, generating a fluorescent signal suitable for tracking sup-tRNA biodistribution in vivo. (**B**) Intratracheal dosing and analysis workflow for delivering tRNA_Aptamer encapsulated within LNPs into mouse lungs with three doses at 1 mg/kg. (**C** and **D**) Uniform manifold approximation and projection (UMAP) plots (C) and corresponding pie charts (D) to describe the identity and percentage of tRNA_Aptamer-positive cells in mouse lungs after delivery by TTP-3 or MC3 LNP formulations. $n = 3$ biological replicates. Data in the pie charts are shown as means. (**E**) Representative flow cytometry histograms and corresponding quantitative analysis comparing the distribution of tRNA_Aptamer-positive cells within epithelial, endothelial, and immune cell populations in mouse lungs. $n = 3$ biological replicates. (**F**) Gating schemes of flow cytometry experiments showing representative quantifications of tRNA_Aptamer-positive percentages within epithelial cell subsets, including ciliated cells (acetylated tubulin+), club cells (CCSP+), and basal cells (KRT5+). $n = 3$ biological replicates. (**G**) Representative immunofluorescence imaging of lung sections demonstrating tRNA_Aptamer localization in epithelial subsets in small airways and bronchi. Scale bars, 500 μm (whole-lung overview) and 100 μm (small-airway and bronchial images). Data are means ± SDs. *P* values were calculated by one-way ANOVA with Tukey's multiple-comparison test in (E) and two-tailed unpaired Student's *t* test in (F).

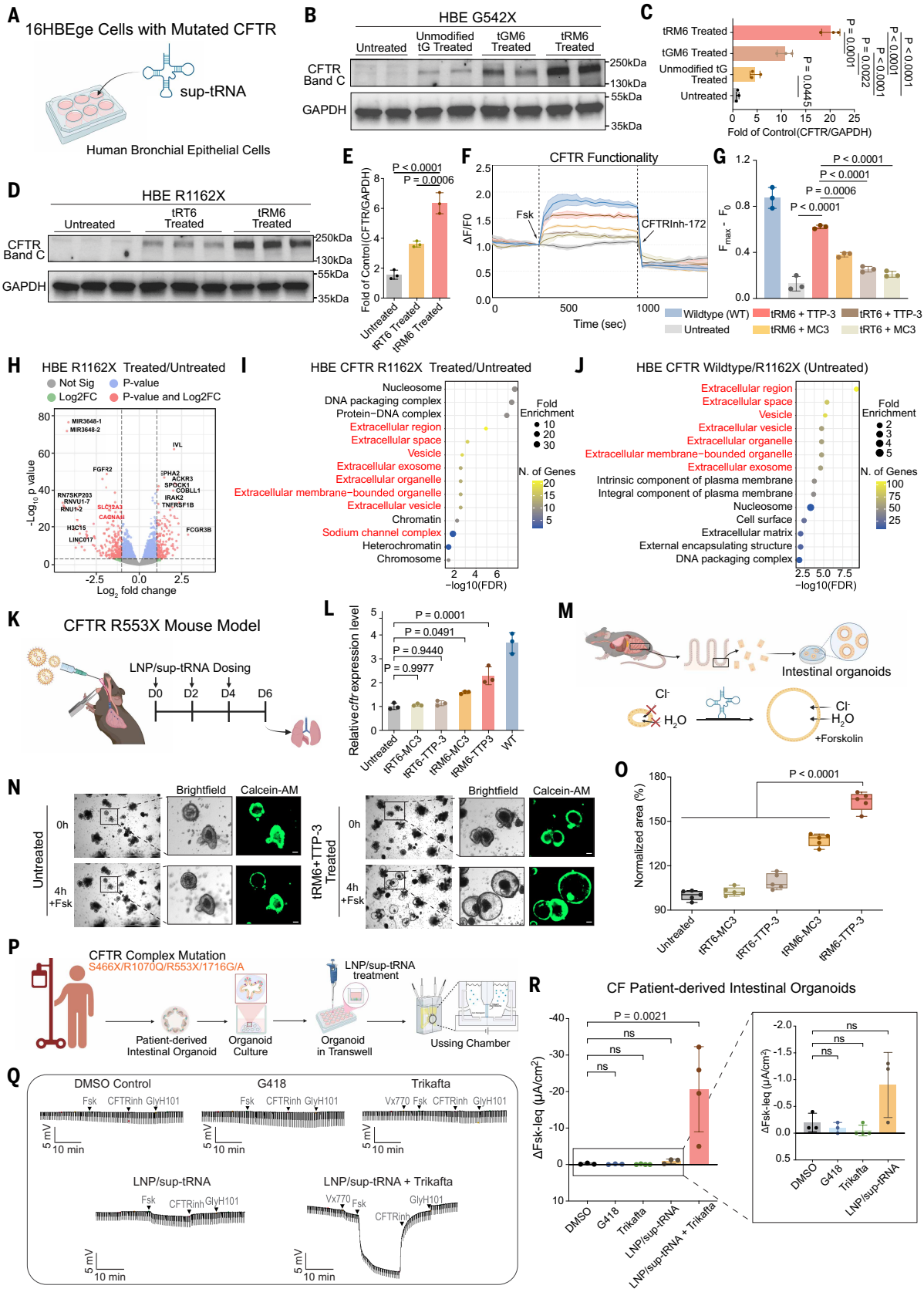

Fig. 5. Therapeutic efficacy of sup-tRNAs in cellular, mouse, and patient-derived CF models. (**A**) Treatment schematic for CFTR-mutant HBE cells. (**B** to **E**) Immunoblot and densitometric quantification of CFTR restoration in HBE G542X [(B) and (C)] and HBE R1162X [(D) and (E)] cells after treatment. (**F** and **G**) Representative FLIPR traces and quantification of forskolin-stimulated CFTR activity in HBE R1162X cells. (**H** to **J**) Poly(A)-RNA-seq analysis. [(H) and (I)] Treated versus untreated HBE R1162X cells. (J) Untreated WT HBE cells versus untreated HBE R1162X cells. In the volcano plot (H), vertical dashed lines depict a twofold change, and horizontal dashed lines indicate adjusted

$P < 0.05$. Hierarchical clustering and gene ontology enrichment of differentially expressed genes. (**K** and **L**) Intratracheal dosing scheme in CFTR R553X mice and lung CFTR mRNA expression after treatment. (**M**) Experimental workflow illustrating ex vivo rescue of CFTR function in intestinal organoids derived from R553X homozygous CF mice. (**N** and **O**) Representative brightfield and calcein-AM fluorescence images. Quantification of normalized intestinal organoid swelling ($n = 5$). Scale bars for uncropped images, 1 mm. (**P**) Workflow for establishing intestinal organoids from a CF patient with complex *CFTR* mutations and their functionality assessment by Ussing chamber. (**Q**) Representative electrophysiological voltage traces from Ussing chamber assays of patient-derived intestinal organoids treated with DMSO (control), G418, Trikafta, LNP–sup-tRNA, or a combination of LNP–sup-tRNA and Trikafta. (**R**) Quantification of CFTR-mediated ion transport responses as reported by Ussing chamber assays. Data are means ± SDs. For quantifications in (C), (E), (G), and (L), $n = 3$ biological replicates; *P* values were calculated by one-way ANOVA with Dunnett's multiple-comparison test versus the indicated controls. In (R), $n = 3$ or 4 replicates from independently prepared organoid-derived monolayers from one CF participant; *P* values were calculated by one-way ANOVA with Tukey's multiple-comparison test for indicated pairwise comparisons. ns, not significant.

and immune-cell profiling showed a similar pattern, with acute inflammation and leukocyte recruitment peaking early after the administration of higher doses and substantial resolution by day 14 (fig. S25). Serum alanine aminotransferase (ALT) and aspartate aminotransferase (AST) were unchanged across groups, indicating no detectable hepatotoxicity. Together, this supported the tolerability of LNP–sup-tRNA at therapeutic doses, with limited systemic toxicity and transient, dose-dependent pulmonary inflammation.

We then evaluated therapeutic efficacy in vivo using a CFTR R553X mouse model (*62*). Mice received three intratracheal doses of LNP–sup-tRNA treatment. Lung tissues collected 2 days after the final treatment showed that the combination of tRM6 and TTP-3 produced the greatest increase in CFTR mRNA, whereas unmodified tRT6- or MC3-based comparison groups showed weaker rescue (Fig. 5, K and L). Because CF mouse models lack overt lung pathology (*69*), we assessed CFTR functional rescue in intestinal organoids derived from R553X mice (Fig. 5M) (*70*). CFTR activity was assayed through forskolin-induced swelling (FIS), where CFTR-mediated ion and water influx into the organoid lumen was highest after tRM6–TTP-3 treatment and lower in groups with unmodified sup-tRNA or nonoptimized LNPs (Fig. 5, N and O, and fig. S26). The combination of optimally modified tRM6, which enhanced intrinsic PTC readthrough, and the sup-tRNA–tailored TTP-3 LNP, which improved delivery of the RNA cargo, led to the most promising results.

Furthermore, we tested the therapeutic efficacy of sup-tRNAs in organoids derived from a CF patient with complex *CFTR* mutations (S466X/R1070Q/R553X/1716G/A) (Fig. 5P). This variant encompasses multiple classes of CFTR defects, including two nonsense mutations, one missense mutation, and one polymorphism, representing a particularly challenging clinical scenario for therapeutic intervention. The clinically approved CFTR modulator (Trikafta) and the readthrough inducing aminoglycoside G418 were included for comparison. tRM6 and serine sup-tRNA (tSA2T5) (*21*) were used to suppress the nonsense mutations. Ussing chamber measurements showed that neither G418 nor Trikafta alone effectively restored CFTR functionality in patient organoids (Fig. 5Q). These results were consistent with clinical observations where CF patients lacking sufficient full-length CFTR protein production did not benefit from existing CFTR modulators. Class I nonsense mutations reduce or abolish full-length CFTR production, restricting Trikafta-mediated correction and potentiation. Notably, combining LNP–sup-tRNAs with Trikafta led to a significant increase in CFTR function (Fig. 5R). Whereas LNP–sup-tRNAs alone produced only a modest, nonsignificant increase relative to untreated controls, the combination therapy made use of complementary rescue mechanisms: sup-tRNAs restored full-length CFTR protein synthesis, allowing Trikafta to support folding, trafficking, and/or channel activity of the restored protein. This finding showcased a promising complementary therapeutic approach and highlighted the importance of combining therapies to rescue complex CFTR genotypes.

Discussion

Sup-tRNAs offer a compelling RNA-level strategy for treating diseases caused by nonsense mutations by promoting PTC readthrough without altering the genome (*71*, *72*). Unlike gene-editing approaches, sup-tRNAs are reversible and avoid permanent genomic changes, thereby reducing concerns related to unintended off-target editing or germline transmission, and they do not require gene-specific guide RNA (gRNA) optimization. Although mRNA-mediated protein replacement is mutation agnostic within a given gene, sup-tRNA therapy offers distinctive advantages, including restoration of endogenous gene expression, prolonged functional persistence, and broad applicability across diseases, while circumventing side effects from elevated protein levels. Notably, a single sup-tRNA can potentially target the same nonsense mutation across multiple disease-causing genes. For example, arginine-to-UGA nonsense mutations account for ~24% of all known pathogenic PTCs (*1*, *73*), which suggests that a single arginine sup-tRNA could be applied to a wide range of genetic disorders. These features make sup-tRNAs particularly attractive when restoration of native, full-length protein from endogenous transcripts is desired.

In this study, we demonstrated that the site-specific chemical modification substantially improved the therapeutic and safety profiles of sup-tRNAs relative to unmodified sup-tRNAs. When delivered using a tailored, pulmonary-optimized LNP system, these modified sup-tRNAs restored CFTR expression and function across multiple CF disease models, supporting their use for therapeutic nonsense-mutation readthrough. Notably, in a patient-derived organoid model with a complex genotype, cotreatment with modified sup-tRNAs and Trikafta enabled functional rescue of CFTR. In this setting, sup-tRNAs suppressed the nonsense mutations to restore full-length CFTR synthesis, whereas Trikafta supported the folding, trafficking, and activity of CFTR. This complementarity is clinically relevant because CFTR modulators, including Trikafta, require modulator-responsive, full-length CFTR protein to act on, which limits their use for class I nonsense-dominated or complex genotypes. Notably, this study focused on a single CF participant, and it should thus be interpreted as a proof of principle; additional testing in patient-derived models with different genotypes will be needed to support the generalizability of this combination strategy. Nevertheless, these findings support the idea that modified sup-tRNAs could restore full-length CFTR expression for subsequent pharmacological modulation, highlighting the potential of genotype-informed combination therapies for patients underserved by current CFTR therapies. To enable tRNA production at scale, chemically modified sup-tRNAs can be accessed through solid-phase synthesis, enabling control over 5′ termini and site-specific modifications. Other approaches, such as in vitro transcription followed by enzymatic modification (*74*), may further enhance scalability and cost-effectiveness. These manufacturing strategies could support scalable production of modified tRNAs and benefit the broader development of tRNA-based therapeutics.

Through systematic investigation of site-specific RNA modifications, this study offers mechanistic insights into how distinct modifications influence the therapeutic performance of sup-tRNAs. These findings highlight the importance of preserving the native tRNA structure and support structure-informed engineering as a guiding principle for sup-tRNA optimization (*75*, *76*). Although RNA modifications are increasingly recognized as regulators of cellular, developmental, and disease

processes (*77*, *78*), their potential for therapeutic tRNAs has not been fully explored. A limitation of this study is that only a defined subset of modifications was tested. Ongoing investigation into additional RNA modifications, aided by advances in RNA-seq and chemical synthesis, should reveal other modification patterns that enhance efficacy and broaden the therapeutic scope of tRNA-based technologies (*79*, *80*). Additionally, although some modifications may have broad utility across multiple tRNA scaffolds, optimal designs may depend on sequence context, amino acid identity, and disease setting. Clinical translation will also require efficient cell- and/or tissue-specific delivery, support for repeated dosing, and minimizing off-target exposure. Advances in both tRNA engineering and delivery may extend tRNA-based therapeutics beyond nonsense suppression to additional genetic alterations, including missense and frameshift mutations, as well as emerging applications in translational control and tRNA fragment-mediated regulatory pathways (*81*, *82*), helping to lay the foundation for the next generation of tRNA therapeutics.

Materials and methods

tRNA synthesis

Chemically modified sup-tRNAs were synthesized by GenScript using solid-phase RNA oligonucleotide synthesis, incorporating a 5′ monophosphate end and specific RNA modifications as required, followed by RNase-free HPLC purification. Unmodified tRNAs were generated through in vitro transcription (IVT). Sequences are available in table S1 (*14*, *21*). For IVT, DNA oligonucleotides encoding the desired tRNA sequences were purchased from IDT (Integrated DNA Technologies). These DNA templates were amplified using polymerase chain reaction (PCR) using Phusion High-Fidelity DNA Polymerase (NEB, no. M0531S). Amplified DNA products served as templates for IVT performed with the HiScribe T7 RNA Synthesis Kit (NEB, no. E2040), with addition of guanosine monophosphate (GMP) to a final concentration of 1.8 mM to ensure a 5′ monophosphate end. The IVT reaction was incubated at 37°C for 16 hours. IVT products were purified by gel extraction. Specifically, the RNA bands corresponding to the desired length were excised from 10% TBE-Urea gels (Bio-Rad, no. 4566033) with yeast tRNA (Invitrogen, no. 15401011) as a molecular size marker (fig. S1). The excised gel slices were incubated overnight at 37°C in a low-pH buffer (20 mM Tris, 200 mM sodium acetate, 5 mM EDTA, pH 5.0). After overnight incubation, RNA was precipitated by adding sodium acetate to a final concentration of 300 mM, followed by 2.5 volumes of ice-cold 100% ethanol. The samples were mixed thoroughly and stored at −80°C for 1 hour. RNA pellets were then collected by centrifugation, washed once with 70% ethanol, air-dried, and resuspended in ultrapure water. To properly fold the tRNAs, the samples were initially denatured at 80°C in a thermocycler and then gradually cooled to 65°C at a rate of 0.1°C/s. At 65°C, $MgCl_2$ was added to achieve a final concentration of 10 mM. Samples were gently mixed and allowed to cool slowly at the same controlled rate (0.1°C/s) in a thermocycler to room temperature, facilitating RNA folding.

NLuc_PTC reporter cell line construction

The opal stop codon TGA was introduced at amino acid position 160 of NanoLuc (NLuc) (*14*) within the pB-EF1a-Nluc-IRES-Puro plasmid (Addgene no. 130936), generating the pB-EF1a-Nluc V160X-IRES-Puro (PB_PTC_Nluc) construct. This construct was transformed into NEB 10-beta Competent *Escherichia coli* cells (NEB, no. C3019), and glycerol stocks were stored at −80°C for future use. Plasmids used in subsequent experiments and mammalian assays were purified using the PureYield Plasmid Miniprep System (Promega, no. A1222), which includes an endotoxin removal step. Antibiotics required for plasmid maintenance and experimental selection were obtained from InvivoGen. To establish the reporter cell line, BEAS-2B cells were seeded into a 6-well plate at a density of 1×10^6 cells per well. Cells were transfected using FuGENE 6 transfection reagent at a ratio of 3 μl reagent per 1 μg DNA, following the manufacturer's protocol. Each transfection contained 0.2 μg of super PiggyBac transposase vector (System Biosciences) and 0.6 μg of PB_PTC_Nluc plasmid DNA. Three days posttransfection, culture media were replaced with fresh media supplemented with 2 μg/ml puromycin (InvivoGen, no. 58-58-2) to select for transfected cells. After a 24-hour incubation, cells were washed twice with PBS and provided with fresh culture media. The surviving puromycin-resistant cells were termed NLuc_PTC BEAS-2B reporter cells. To test tRNA-induced readthrough and in vitro kinetics study of sup-tRNA variants, these NLuc_PTC reporter cells were transfected using Lipofectamine MessengerMAX (Invitrogen, no. LMRNA008).

Cell culture

Human lung epithelial (BEAS-2B) cells and HBE (16HBE14o-) cells were a gift from J. Hu. CFF-16HBEge CFTR G542X and CFF-16HBEge CFTR R1162X cells were kindly provided by H. Valley and the Cystic Fibrosis Foundation Therapeutics Lab. All epithelial cells were maintained in Eagle's minimum essential medium (MEM) supplemented with 10% fetal bovine serum (FBS) (Gibco) and 1% Penicillin/Streptomycin (Gibco). THP-1 Dual cells (human monocytes) were purchased from InvivoGen (no. thpd-nfis). THP-1 dual reporter cells were maintained in RPMI 1640 (Gibco), 2 mM L-glutamine, 25 mM HEPES, 10% heat-inactivated FBS (Gibco), 100 μg/ml Normocin (InvivoGen, no. ant-nr-1), and 1% Penicillin/Streptomycin (Gibco). Cells were grown in a humidified incubator containing 5% CO_2 at 37°C. All cell lines included in this study were routinely monitored for mycoplasma contamination using mycoplasma PCR detection and consistently found negative.

Immunogenicity reporter assay

THP-1 dual-reporter cells were seeded into a U-bottom 96-well plate at a density of 1×10^5 cells per well. To evaluate the immunogenicity of tRNA variants, cells were treated with either LNP-encapsulated sup-tRNA or an empty LNP control. After 24 hours of incubation at 37°C, 20 μl of cell supernatant was mixed with 180 μl of QUANTI-Blue reagent (InvivoGen, no. rep-qbs) and incubated for 1 hour. The optical density (OD) at 630 nm was measured using a Cytation 1 Cell Imaging Multimode Reader (BioTek) to quantify SEAP activity, indicative of NF-κB pathway activation. Simultaneously, another 20 μl of the supernatant was combined with 50 μl of QUANTI-Luc reagent (InvivoGen, no. rep-qlc1) in a white opaque plate, and luminescence was measured using the same Cytation 1 plate reader. Luminescence values were reported as relative luminescence units (RLUs) and correspond to IRF pathway activation.

Acid-urea polyacrylamide gel electrophoresis (PAGE) for in vitro aminoacylation assay

Aminoacylation reactions using 2 μg tRNA were performed with 100 mM Hepes (pH 7.5), 20 mM KCl, 2 mM dithiothreitol (DTT), 10 mM MgCl2, 1 mM adenosine 5′-triphosphate (ATP), and 2 μM purified recombinant human GARS1. tRNAs were aminoacylated at 37°C for 30 min and samples were then mixed with 2× acidic RNA loading dye (8 M urea, 0.05% bromophenol blue, 0.05% xylene cyanol FF, and 0.1 M NaOAc, pH 5). Charged and uncharged tRNA were separated by a 20 cm acidic denaturing PAGE [4% stacking and 6.5% running (19:1) acrylamide:bisacrylamide, 8 M urea, and 0.1 M NaOAc, pH 5] at 4°C. tRNAs were then visualized with SYBR Green II RNA Gel Stain (Invitrogen, no. S7564).

Radiolabeled aminoacylation assay

Samples containing 100 mM Hepes (pH 7.5), 20 mM KCl, 2 mM DTT, 10 mM MgCl2, 1 mM ATP, 20 μM L-arginine, 5 μM L-[3H] arginine and 5 μM tRNA were initiated with 4 μM purified recombinant human RARS1 and incubated at 37°C. Aliquots were removed at specified time points and quenched into filter plates containing 0.5 mg/ml sheared DNA and 100 mM EDTA in 300 mM NaOAc (pH 3). tRNA was then

precipitated using 20% cold trichloroacetic acid and washed four times with a cold solution of 5% trichloroacetic acid and 100 mM L-Arginine. The filter plates were then dried after a rinse with 95% ethanol. Aminoacyl-tRNAs were hydrolyzed with 0.1 M NaOH to release radiolabeled amino acids, which were spun into white 96-well plates with OptiPhase HiSafe 3 (Revvity) for scintillation counting on a Hidex Sense Beta Plus Microplate Reader (*83*).

Kinetics study

For the in vitro kinetics study, reporter cells were seeded at a density of 2×10^4 cells per well in 96-well plates. After 24 hours (designated day 0), cells were transfected with 500 ng of either unmodified or chemically modified sup-tRNA using Lipofectamine MessengerMAX (Invitrogen, no. LMRNA008). Twenty-four hours after transfection, the medium in all wells was replaced with fresh culture medium to remove residual Lipofectamine reagent. At the indicated time points, luminescence was measured from four wells per condition using the Nano-Glo Luciferase Assay System (Promega, no. N1120) on a Cytation 1 plate reader (BioTek). Luminescence values were normalized to untreated control wells at each time point.

For the in vivo kinetics studies, LumA-PTC mice (~4 weeks old) were administered with SM-102 LNP-encapsulated unmodified or modified sup-tRNA via tail vein injection at a dose of 1.25 mg/kg. SM-102 LNPs were selected for their liver-targeting properties and were formulated with ionizable lipid/DSPC/cholesterol/PEG-lipid at a molar ratio of 50/10/38.5/1.5. At the indicated time points, mice were injected intraperitoneally with 0.2 ml D-luciferin solution (10 mg/ml in DPBS; PerkinElmer). For whole-body luminescence imaging, the same batch of mice (without sacrificing) were anesthetized with 2.5% isoflurane in oxygen and imaged 10 min after luciferin injection. Luminescence signals from the liver region were acquired and quantified using an in vivo imaging system (IVIS) (PerkinElmer).

tRNA-seq library preparation and analysis

tRNA-seq was performed on 16HBEge cells expressing CFTR R1162X under three conditions in three biological replicates: untreated, treated with modified sup-tRNA (tRM6), or treated with unmodified sup-tRNA (tRT6). Cells were seeded in 6-well plates at a density of 1.5×10^6 cells per well. Twenty-four hours after seeding (day 0), cells in the treatment groups received either tRM6 or tRT6 at 2 μg per well. Untreated cells harvested on day 1 served as the negative control. Samples were collected on days 1, 7, 14, 21, and 35 for the tRM6-treated group, and on days 1, 14, and 35 for the tRT6-treated group. For collections beyond day 14, cells were passaged from the original 6-well plates into 100-mm Petri dishes to prevent overconfluence-associated cell death. At each designated time point, cells were washed with cold PBS twice, and total RNA was extracted using TRIzol reagent (Invitrogen, no. 15596026). Small RNA-seq libraries were generated following the protocol described by a previous study (*84*), with minor modifications. Total RNA was isolated from all samples as described above, using 1 μg of total RNA per sample as input. To preserve the aminoacylation state, RNA was maintained under acidic conditions throughout the preparation. Total RNA underwent a one-pot periodate oxidation and β-elimination reaction to selectively remove the terminal 3′ nucleotide from uncharged tRNAs. This was followed by 3′ end repair using T4 polynucleotide kinase (NEB). Subsequently, barcoded, biotinylated capture hairpin oligonucleotides were ligated to RNA 3′ ends using T4 RNA ligase I (NEB). Samples were then pooled and immobilized on streptavidin-coated MyOne C1 Dynabeads (ThermoFisher). All downstream processing steps were carried out on-bead, including dephosphorylation, reverse transcription with SuperScript IV VILO (ThermoFisher) under extended incubation conditions, RNase H digestion (NEB), periodate oxidation to inactivate unligated adapters, and second adapter ligation. Libraries were amplified by PCR using Q5 high-fidelity DNA polymerase, followed by size selection using 10% Tris–borate-EDTA PAGE (Invitrogen) to remove terminal transferase by-products. DNA was then purified via gel extraction and ethanol precipitation. Final libraries were sequenced on the Illumina NovaSeq X platform using paired-end sequencing by the Centre for Applied Genomics at the Hospital for Sick Children. Data analysis was performed as described in a previous study (*85*), with computational support from the Trillium high-performance computing cluster operated by the University of Toronto and Compute Canada. Briefly, paired-end reads were merged and aligned to human tRNA reference sequences using Bowtie2 (*86*). Reads at each nucleotide position were quantified using the pileup function in Samtools (*87*), and tRNA-level read counts were determined using Pysam as previously described (*85*). Differential expression analysis was conducted using DESeq2 (*88*). Modifications were called as the percentage of mismatches and terminations at the position of interest and were quantified from Samtools pileup files using RStudio. Aminoacylation levels were determined through counts of intact CCA over the first C, with reads quantified from Samtools pileup files. All computational analyses were performed on the Trillium high-performance computing cluster (University of Toronto, Compute Canada) or using RStudio.

Ionizable lipid library synthesis

A library of 1000 ionizable lipids was synthesized using the Ugi four-component reaction (Ugi-4CR) using amine headgroups (–NH_2), aldehyde linkers (–CHO), carboxylic acid tails (–COOH), and isocyanide tails (–NC). All reagents were purchased from Tokyo Chemical Industry (TCI) or Sigma-Aldrich. The isocyanide tails were purified using gradient chromatography with ethyl acetate and hexane, and their structures were confirmed by proton nuclear magnetic resonance (^{1}H NMR) spectroscopy in $CDCl_3$. For high-throughput combinatorial screening, reaction components were individually dissolved in methanol and combined at a 1:1:1:1 molar ratio (amine:aldehyde:carboxylic acid:isocyanide) in 96-well PCR plates. The reaction was carried out overnight at room temperature in plates while continuously shaking. The final TTP-3 ionizable lipid was purified with a gradient of MeOH and DCM; lipid purity and identity were validated by 1H NMR spectrometry [1H NMR (400 MHz, CDCl3) δ 5.41 – 5.24 (m, 4H), 4.01 (d, J = 2.6 Hz, 2H), 3.68 (s, 1H), 3.39 (s, 1H), 3.23 (s, 1H), 3.04 (s, 1H), 2.73 (d, J = 3.5 Hz, 2H), 2.45 (d, J = 16.8 Hz, 1H), 2.34 – 2.13 (m, 11H), 2.01 (dd, J = 7.0, 2.9 Hz, 4H), 1.65 – 1.20 (m, 45H), 1.00 (d, J = 3.2 Hz, 6H), 0.84 (dtd, J = 7.3, 4.3, 2.2 Hz, 9H)].

Preparation of LNPs

For high-throughput screening, LNPs were formulated using an automated OT-2 liquid handling system (Opentrons). The process involved mixing an aqueous phase containing sup-tRNA in 10 mM citrate buffer (pH 4.0, Fisher) with an organic lipid phase at a volume ratio of 3:1 and an ionizable lipid-to-RNA mass ratio of 10:1. The organic phase comprised synthesized ionizable lipids mixed with helper lipids: DOPE (Avanti, no. 850725P), cholesterol (Sigma-Aldrich, no. C8667), and C14-PEG2000 (Avanti, no. 880150P), dissolved in ethanol at a molar ratio of 35:16:46.5:2.5. For in vivo applications, LNPs were produced by mixing aqueous sup-tRNA solutions with the organic lipid phase using a T-junction device operated with syringe pumps at a minimum volume of 300 μl. Subsequently, the LNP suspensions were dialyzed against PBS overnight at 4°C using 100 kDa MWCO dialysis cassettes (Spectra/Por, ThermoFisher, no. 132670). Postdialysis, LNPs were concentrated by centrifugation in 100 kDa MWCO Amicon Ultra-0.5 centrifugal filters (Millipore, no. UFC510096). For optimized TTP-3 LNP formulation, the organic phase was prepared by dissolving TTP-3 ionizable lipids with helper lipids: DOPE (Avanti, no. 850725P), β-sitosterol (ApexBio, no. B6199), and C14-PEG2000 (Avanti, no. 880150P) in ethanol at a molar ratio of 60:10:27.5:2.5. The aqueous phase containing sup-tRNA in 10 mM citrate buffer (pH 4.0) was mixed with the organic phase at a 3:1 volume ratio, maintaining an ionizable lipid-to-tRNA

mass ratio of 13.5:1. In the formulation optimization study, additional helper lipids evaluated included DSPC (Avanti, no. 850365P) and DOTAP (Avanti, no. 890890P). Sterol lipids tested comprised cholesterol (Sigma-Aldrich, no. C8667) and β-sitosterol (ApexBio, no. B6199).

ALI culture

Preparation of ALI cultures using BEAS-2B cells followed the STEMCELL Technologies protocol. Briefly, BEAS-2B cells were first enzymatically detached using 0.05% trypsin-EDTA (Thermo Fisher Scientific) from the culture flask and seeded onto the apical side of PET Transwell inserts (0.4 μm pore size, 6.5 mm diameter; Corning, no. 3470) in 24-well plates at a density of 2.0×10^4 cells/cm^2. Initially, PneumaCult complete base medium (STEMCELL Technologies, no. 05001) was added at volumes of 0.2 ml to the apical compartment and 0.5 ml to the basal compartment. Upon reaching confluency, cultures were transitioned to ALI conditions by removing the apical medium and supplying PneumaCult maintenance medium (STEMCELL Technologies, no. 05001) exclusively to the basal compartment, with medium changes every 2 days. After 28 days under ALI conditions, cells were prepared for LNP transfection. 5 μl of artificial sputum medium (Biochemazone, no. BZ316) was applied to the surface of differentiated cultures to mimic airway mucus before LNP transfection.

LNP formulation optimization

A DoE approach was used to optimize key formulation parameters known to affect LNP transfection efficiency, as measured by sup-tRNA readthrough activity. Seven independent variables were systematically evaluated: (i) ionizable lipid-to-tRNA mass ratio (7.5 to 20), (ii) ionizable lipid molar ratio (30 to 60%), (iii) helper lipid type (DSPC, DOPE, DOTAP), (iv) helper lipid molar ratio (10 to 30%), (v) sterol lipid type (cholesterol, β-sitosterol), (vi) sterol lipid molar ratio (7.5 to 59.5%), and (vii) PEGylated lipid molar ratio (0.5 to 2.5%). A total of 38 distinct formulations were generated by the JMP 17.0 software (SAS Institute), encompassing a diverse range of parameter combinations to enable robust statistical analysis. Each formulation was tested for sup-tRNA delivery efficiency, and the obtained results were subsequently input into JMP for further statistical modeling and analysis. This process identified the formulation exhibiting optimal performance based on statistically significant differences. Detailed formulations and analysis outcomes are summarized in table S2. All RNA doses used in the main experiments are summarized in table S3.

Animal experiments

All animal studies were reviewed, approved, and performed in accordance with guidelines established by the University Health Network Animal Resources Centre (ARC), under the approved animal use protocol AUP6856. C57BL/6 mice aged 4 to 8 weeks were purchased from the Jackson Laboratory. Breeding pairs of homozygous C57BL/6J-*Gt(ROSA)26Sor*^{em1Crx}/J (LumA-PTC) mice were obtained from the Jackson Laboratory (no. 038165), and colonies were maintained at ARC. Additionally, breeding pairs of heterozygous Cftrem9Cwr (human exon 12 replacement-R553X) mice were generously provided by C. A. Hodges from the Cystic Fibrosis Mouse Resource Center, Case Western Reserve University. These colonies were subsequently expanded and maintained at ARC.

Nebulization of LNPs

To evaluate the impact of nebulization on LNP–sup-tRNA formulations, an Aeroneb Lab Control Module with a laboratory nebulizer unit (Aerogen, no. NEB-0801) was used as previously described (*56*, *57*). LNP solutions (150 μl), dialyzed against DPBS overnight at 4°C using 100 kDa MWCO dialysis cassettes (Spectra/Por, Thermo Fisher, no. 132670), were subjected to nebulization. The generated aerosol was collected by condensation into 1.5 ml microcentrifuge tubes, allowing recovery of LNPs in liquid phase for downstream analysis. Collected nebulized LNPs were applied to BEAS-2B reporter cells under standard culture conditions. Pre- and postnebulized formulations were prepared using the same initial LNP composition. Total and encapsulated RNA concentrations were quantified using a RiboGreen assay. Briefly, total RNA was measured after disruption of LNPs with Triton X-100, and encapsulated RNA was determined from intact particles. These measurements were used to estimate RNA recovery and guide dosing in subsequent cell-based assays.

LNP characterization

Hydrodynamic diameter and polydispersity index (PDI) were measured by dynamic light scattering (DLS) and reported as the intensity-weighted Z-average diameter and PDI using a Malvern Zetasizer. Zeta potential measurements were conducted at 1 ng/μl LNP concentration in DPBS using Malvern Zetasizer. Encapsulation efficiency (EE) was assessed via a RiboGreen Assay as previously described (*49*). Briefly, LNP samples were either lysed with 10% Triton X-100 in TE buffer at 37°C for 30 min or diluted directly in TE buffer without lysis. Each sample (100 μl) was combined with an equal volume of RiboGreen reagent (1:200 dilution) in a 96-well plate and incubated for 5 min at room temperature in the dark. Fluorescence intensity (excitation/emission: 485/528 nm) was measured using a Cytation 1 plate reader (BioTek). Standard curves generated from known RNA concentrations in TE and TE/Triton-X100 buffers were used to quantify free and total RNA. Encapsulation efficiency was calculated as: EE% = (Conc. total RNA – Conc. free RNA)/Conc. total RNA × 100%.

LNP diffusivity assay

Microchannels of Ibidi μ-Slide VI 0.4 (Ibidi no. 80601) were filled with 40 μl of artificial mucus, followed by the addition of DiI-labeled (Invitrogen, no. D282) LNPs encapsulating sup-tRNA. LNP diffusion within the mucus matrix was imaged after 1 hour using a Zeiss Axio Imager microscope. Diffusion across the channel was semiquantified by measuring fluorescence intensity along the microchannel.

Aptamer-incorporated tRNA

RNA Mango II aptamer (gaaggagaggagaggaagaggaga) without the clamping region was inserted into the variable loop of the sup-tRNA to build tRNA_Aptamer. The preservation of the tRNA structure despite the inserted aptamer and isotype-specific model scores were confirmed by tRNAscan-SE 2.0 (*89*, *90*). The functional impact of aptamer insertion was assessed by measuring readthrough activity in NLuc_PTC reporter cells. Cell viability assays showed no increase in cytotoxicity associated with aptamer incorporation. Thus, the Mango II–modified sup-tRNA was used as a fluorescent tracking probe for in vivo biodistribution studies.

Single-cell suspension from mouse lungs

Mouse lungs (including the trachea) were harvested and placed in PBS containing 2% FBS. Lung tissues were minced into a homogeneous paste and transferred into 10 ml dissociation medium composed of Dulbecco's modified Eagle's medium (DMEM) supplemented with 300 U/ml collagenase IV and 100 U/ml deoxyribonuclease (DNase) I. Samples were incubated at 37°C for 40 min on a shaking platform. After incubation, the tissue digest was passed through a 70 μm nylon mesh strainer using the rubber end of a syringe plunger to create a single-cell suspension. The strainer was rinsed with an additional 10 ml of PBS with 2% FBS. Cells were then pelleted by centrifugation at 300*g* for 8 min. After aspirating the supernatant, the cell pellet was resuspended in 5 ml RBC lysis buffer (Invitrogen, no. 00433357) and incubated for 8 min at room temperature to lyse red blood cells. The reaction was quenched by adding 10 ml of PBS with 2% FBS, followed by centrifugation at 300*g* for 5 min. The resulting cell pellet, free of red blood cells, was resuspended in 5 ml of cell staining buffer and prepared for subsequent flow cytometry analysis.

Flow cytometry

Single-cell suspensions derived from mouse lungs were initially incubated with anti-CD16/32 antibody (BioLegend, no. 101302) for Fc receptor blocking. Subsequently, cells were stained on ice for 40 min with the following surface markers: Alexa Fluor 488 anti-mouse CD326/Ep-CAM (BioLegend, no. 118210, 1:100), Brilliant Violet 421 anti-mouse CD45 (BioLegend, no. 147719, 1:150), PE/Cyanine7 anti-mouse CD31 (BioLegend, no. 102524, 1:150), and Zombie NIR Fixable Viability Kit (BioLegend, no. 423106, 1:1000). After staining, cells were washed twice with PBS and fixed on ice for 50 min using Fix Buffer (BD Bioscience, no. 554714). Fixed cells were pelleted by centrifugation at 300*g* for 5 min and washed with Permeabilization Buffer (BD Bioscience, no. 554714). Cells designated for intracellular staining were incubated for 40 min with one of the following antibodies diluted in permeabilization buffer: acetylated alpha Tubulin antibody (6-11B-1) Alexa Fluor 647 (Santa Cruz, no. sc-23950, 1:150), CCSP antibody (B-6) Alexa Fluor 488 (Santa Cruz, no. sc-390313, 1:150), or cytokeratin 5 antibody (RCK103) Alexa Fluor 488 (Santa Cruz, no. sc-32721, 1:150), anti-mouse FOXI1 antibody Alexa Fluor 647 (Novus Biologicals, no. NBP2-70747). After incubation, cells were washed again with Permeabilization Buffer. Cells stained for cell-surface markers were resuspended in PKM buffer (10 mM sodium phosphate, 140 mM KCl, 1 mM $MgCl_2$) supplemented with TO3-3PEG-Biotin (Applied Biological Materials, no. G959, 1:100). For intracellular marker analysis, cells were resuspended in PKM buffer containing either TO1-3PEG-Biotin (Applied Biological Materials, no. G955, 1:100) or TO3-3PEG-Biotin, selected to avoid spectral overlap with the antibody fluorophore used in each panel. AF488-conjugated antibodies (CCSP and KRT5) were paired with TO3, whereas AF647-conjugated antibodies (acetylated α-tubulin and FOXI1) were paired with TO1: TO1-3PEG-Biotin with mango aptamer (ex/em: 510/535) and TO3-3PEG-Biotin with mango aptamer (ex/em: 615/658). Cells were incubated for 30 min, washed, and resuspended in PBS for flow cytometric analysis (*91*). Experiments were performed with appropriate compensation using single-color controls, and signals were collected using distinct detector settings on the flow cytometer. Data acquisition was performed on a CytoFlex S flow cytometer, and analyses were conducted using FlowJo 10.10.0 software. All antibodies used in this study are listed in table S4.

Immunofluorescence staining

Mouse lungs were washed with PBS, fixed in 4% paraformaldehyde (PFA) for 24 hours, and dehydrated in 30% sucrose solution for 48 hours. The tissues were embedded in OCT, frozen, and sectioned at 10 μm thickness using a Leica CM3050S cryostat. Sections were mounted on charged slides, washed with PBS, blocked, and permeabilized using blocking buffer [PBS containing 5% bovine serum albumin (BSA) and 0.1% Triton X-100] for 1 hour at room temperature. Sections were incubated overnight at 4°C with one of two antibody combinations: acetylated alpha Tubulin Antibody (6-11B-1) Alexa Fluor 488 (Santa Cruz, no. sc-23950, 1:100) and CCSP antibody (B-6) Alexa Fluor 647 (Santa Cruz, no. sc-39031, 1:100), or CCSP antibody (B-6) Alexa Fluor 488 (Santa Cruz, no. sc-39031, 1:100) and cytokeratin 5 Antibody (RCK103) Alexa Fluor 594 (Santa Cruz, no. sc-32721, 1:100). After antibody staining, slides were washed three times with PBS and incubated with 4′,6-diamidino-2-phenylindole (DAPI) (Roche, no. 10236276001, 1:1000) for 20 min at room temperature. After another PBS wash, sections were incubated with PKM buffer (10 mM sodium phosphate, 140 mM KCl, 1 mM $MgCl_2$) containing either TO1-3PEG-Biotin (Applied Biological Materials, no. G955, 1:100) or TO3-3PEG-Biotin (Applied Biological Materials, no. G959, 1:100) for 30 min at room temperature, followed by a final PBS wash. Upon binding to the Mango aptamer, TO1-3PEG-Biotin and TO3-3PEG-Biotin exhibited fluorescence with excitation/emission maxima of 510/535 nm and 615/658 nm, respectively. Slides were mounted with mounting medium (Epredia, no. 4112) and imaged using a Leica Stellaris 5 Confocal microscope (AOMF, UHN).

Immunoblot

16HBEge cells, with different CFTR mutations or 16HBE14o- WT CFTR, were seeded in 6-well plates at density of 1.0×10^6 cells per well for sup-tRNA treatment with three dosages in total (1.25 μg per well) administered every other day. One day after the last dosage, cells were washed with PBS and lysed using 1× RIPA buffer (Cell Signaling, no. 9806) supplemented with protease inhibitors (Roche, no. 04693159001) at 4°C for 30 min with gentle agitation. Lysates were clarified by centrifugation at 12,000*g* for 20 min at 4°C, and protein concentrations were determined using a Pierce BCA Protein Assay Kit (Thermo Fisher Scientific, no. 23227). Normalized protein lysates, mixed 1:1 with 4× Laemmli sample buffer (Bio-Rad, no. 1610747), were separated on 4 to 15% Mini-PROTEAN TGX precast gels (Bio-Rad, no. 4561084) alongside a PageRuler Plus Prestained Protein Ladder (10 to 250 kDa, Thermo Fisher Scientific, no. 26619). Proteins were transferred on nitrocellulose membranes using the Bio-Rad TransBlot Turbo system. Membranes were blocked overnight at 4°C with EveryBlot blocking buffer (Bio-Rad, no. 12010020) and incubated overnight at 4°C with monoclonal CFTR-NBD2 antibody (UNC, no. 596, 1:2000). After washing with TBS-T, membranes were incubated with HRP-conjugated goat anti-mouse secondary antibody (BioLegend, no. 405306, 1:5000) for 45 min at room temperature. After additional washing, membranes were developed for imaging. Membranes were subsequently reprobed with anti-GAPDH antibody (BioLegend, no. 649202, 1:1000) for 1 hour at room temperature, followed by incubation with the same secondary antibody. Immunoblot signals were quantified using ImageJ software.

RNA-seq and analysis

RNA-seq was performed on three experimental groups: untreated 16HBEge cells expressing CFTR R1162X (untreated), 16HBEge cells expressing CFTR R1162X treated with tRM6 (treated), and WT CFTR 16HBE14o- cells (WT). Cells were seeded in 6-well plates at a density of 1.5×10^6 cells per well. The treated group received three doses of sup-tRNA (1.25 μg per well), administered every other day. One day after the final treatment, cells were washed with PBS, and total RNA was extracted using TRIzol reagent (Invitrogen, no. 15596026), followed by isopropanol precipitation. Poly(A)$^+$ RNA was enriched from total RNA using the NEBNext Poly(A) mRNA Magnetic Isolation Module (NEB, no. E7490S) according to the manufacturer's instructions. RNA-seq libraries were constructed using the NEBNext Ultra II RNA Library Prep Kit for Illumina (NEB, no. E7770S), incorporating USER enzyme (NEB, no. M5505S) during adaptor ligation to open the hairpin-loop structure. Sequencing was performed at the Donnelly Sequencing Centre in Toronto on a Novaseq6000 SP 200c at >35 million reads per sample and 100 nucleotide (nt) read length. Data analysis was enabled by computational infrastructure provided by Compute Ontario, SciNet, and the Digital Research Alliance of Canada. In brief, reads were trimmed and quality controlled with Trimgalore, aligned against GRCh38 with STAR aligner (*92*), and differentially expressed mRNAs were determined with DESeq2 (*88*), version 1.38.3. Gene ontology (GO) analysis and molecular pathway enrichment were conducted using ShinyGO 0.82 (South Dakota State University) (*93*).

Ribosome profiling library preparation and analysis

Ribosome profiling libraries were prepared using the QEZ-seq kit (EzraBio, no. 2603001-6) according to the manufacturer's instructions (*94*). 16HBEge cells expressing CFTR R1162X were analyzed in two experimental groups: untreated or treated with modified sup-tRNA (tRM6), with three biological replicates per group. Cells were seeded in 6-well plates at a density of 1.5×10^6 cells per well. Twenty-four hours after seeding, cells in the treatment group received sup-tRNA dosing at 2 μg per well. Untreated and sup-tRNA–treated cells were harvested 24 hours after the treatment. At harvest, cells were rapidly cooled on ice and lysed in ice-cold ribosome-protected fragment (RPF) lysis buffer containing cycloheximide to stabilize translating

ribosomes. Lysates were clarified by centrifugation, and ribosome-protected fragments were generated by nuclease digestion at 4°C according to the QEZ-seq workflow. After digestion, RNA was extracted using TRIzol LS reagent (Invitrogen) and ethanol precipitated. Ribosome-protected fragments were size selected by 15% denaturing PAGE, and fragments corresponding to monosomes (~30 nt) were excised and purified. Size-selected RNA fragments were resuspended in nuclease-free water and quantified before library preparation. Library construction was performed using the QEZ-seq workflow. Briefly, RNA fragments were subjected to 3′ adenylation followed by ligation of sequencing adapters. Adapter-ligated RNA was immobilized on streptavidin-coated magnetic beads and processed on-bead through reverse transcription using the supplied reverse transcription mixture under optimized incubation conditions. After cDNA synthesis, RNA was removed enzymatically, and libraries were amplified by PCR using barcoded primers provided in the kit. Amplified libraries were size selected (~180 base pairs, corresponding to insert plus adapters) by 10% TBE-PAGE to remove by-products, followed by gel extraction and ethanol precipitation. Final libraries were sequenced on Illumina's NovaSeq X platform using paired-end sequencing at The Centre for Applied Genomics at the Hospital for Sick Children. Sequencing data were processed using a ribosome profiling analysis pipeline adapted from standard workflows (*94*). Paired-end reads were adapter-trimmed and filtered with Cutadapt (*95*) using parameters: -a AAAAAAAAAA-AAAAAA and -g GGG for 3′ and 5′ trimming, respectively. A maximum error rate of 10% was allowed during adapter matching, and reads shorter than 15 nt were excluded from analysis. Trimmed reads were aligned to rRNA reference sequences using Bowtie2 (*86*) to remove rRNAs, and unmapped reads were retained for downstream analysis. The remaining reads were then aligned to the human genome (hg38) using STAR (*92*). Read distributions across 5′UTRs, coding sequences (CDS), and 3′UTRs were quantified using the RiboProfiling and RibosomeProfilingQC R packages (*96*). Canonical ribosome-protected fragment lengths (28 to 33 nt) were used for quality control analyses, including metagene coverage profiling to evaluate ribosome occupancy across transcript regions, with reads binned by 5′UTRs, CDS, and 3′UTRs. Additionally, strand bias, transcript region distribution, and periodicity were assessed. Gene-level read counts were quantified from aligned BAM files, and differential ribosome occupancy between conditions was assessed using DESeq2 (*88*). All computational analyses were performed on the Trillium high-performance computing cluster (University of Toronto, Compute Canada) or with RStudio.

Reverse transcription quantitative PCR (RT-qPCR)

Total RNA was isolated using TRIzol reagent (Invitrogen, no. 15596026), followed by precipitation with isopropanol. RNA was reverse transcribed using SuperScript IV Reverse Transcriptase (Thermo Fisher Scientific, no. 18090050) with 50 μM random hexamer primers. qPCR was performed using Power SYBR Green PCR Master Mix (Thermo Fisher Scientific, no. 4367659). Primers used for qPCR are listed in table S5. Data were analyzed using the ΔΔCT method. Each biological replicate was assayed in technical duplicates.

FLIPR membrane potential assay

Cells were seeded into black wall, clear bottom 96-well plates for three dosages (500 ng per well). Before the assay, cells were washed with PBS and then incubated with 0.5 mg/ml blue membrane potential dye (FLIPR Membrane Potential Assay Kit; Molecular Devices) dissolved in chloride-free buffer (10 mM glucose, 20 mM HEPES, 136 mM sodium gluconate, 3 mM potassium gluconate, pH 7.35, 300 mOsm) for 30 min at 37°C. Plates were subsequently transferred to a fluorescent microplate reader (SpectraMax i3X Multi-Mode Microplate Reader; Molecular Devices) maintained at 37°C. Baseline fluorescence (excitation 530 nm; emission 560 nm) was recorded, forskolin (10 μM, Sigma-Aldrich, no. F6886) was then added, and fluorescence was monitored to determine the forskolin-stimulated response. CFTRinh-172 (10 μM, Sigma-Aldrich, no. C2992) was then added to confirm CFTR-dependent signal. CFTR activity was quantified as the forskolin-induced change in fluorescence relative to baseline.

In vivo safety evaluation

C57BL/6J (6 weeks old) female mice from the Jackson Laboratory were used. For pulmonary safety assessment, mice were administered LNP–sup-tRNA via intratracheal instillation at doses of 1, 3, 5, or 10 mg/kg on day 0. PBS was used as a negative control, and lipopolysaccharide (LPS) (5 μg per mouse) served as a positive inflammatory control. Samples were collected at multiple time points to evaluate both acute and subacute responses. BALF was collected at 4 hours, day 1 (D1), and day 14 (D14) postadministration, depending on the endpoint. Briefly, lungs were lavaged with sterile PBS, and recovered fluid was used for downstream analyses. Blood was collected via cardiac puncture, and serum was isolated by centrifugation. Cytokine levels in BALF and serum were quantified using a Luminex multiplex assay (Eve Technologies). Complement activation was assessed by measuring C5a and C3a levels in BALF at 4 hours postadministration using ELISA kits (C5a: RayBiotech, no. ELM-CCC5a-1; C3a: Invitrogen, no. EEL091). BALF cellular composition was analyzed at 24 hours after intratracheal administration of the LNP–sup-tRNA treatment. Lung tissues were harvested at D1 and D14, fixed in formalin, embedded in paraffin, sectioned, and stained with hematoxylin and eosin (H&E) for histopathological evaluation.

Intestinal organoid culture from isolated mouse intestinal crypts and treatment

Intestinal organoids were generated from R553X mice following established methods. Briefly, mice were euthanized, and ~20 cm of small intestine proximal to the stomach was harvested, flushed with PBS, and cut open longitudinally. The intestinal segments were further sectioned into ~2 mm pieces and washed thoroughly until the supernatant was clear. Tissue pieces were resuspended in 25 ml Gentle Cell Dissociation Reagent (STEMCELL Technologies, no. 100-0485) and incubated at room temperature on a rocking platform at 50 rpm for 15 min. After incubation, tissues were resuspended in 10 ml cold PBS containing 0.1% BSA, filtered through a 70 μm cell strainer, and collected into four fractions. Fractions enriched in crypts (fractions 2 to 4) were identified microscopically, pelleted, and resuspended in a 1:1 mixture of Matrigel (Corning, no. 354234) and IntestiCult Organoid Growth Medium (mouse) (STEMCELL Technologies, no. 06005). Approximately 50 μl aliquots containing ~1500 crypts were plated into the center of wells in prewarmed 24-well plates. After solidification at 37°C for 15 min, 750 μl complete IntestiCult Organoid Growth Medium (mouse) was added. Organoids were cultured at 37°C with 5% CO_2, with medium changed every 2 days and organoids passaged every 7 days. Upon reaching ~75% confluency, organoids were released from Matrigel, centrifuged, and enzymatically dissociated into single cells using Accutase (Gibco, no. A1110501). Digestion was halted by adding DMEM supplemented with 10% FBS. Single-cell suspensions (3×10^4 cells per well) in IntestiCult Organoid Growth Medium (mouse) were seeded into Matrigel-coated 96-well plates and treated with LNP–sup-tRNA every other day at a dosage of 500 ng per well, for a total of three treatments. Cells were cultured for 4 to 5 days until fully formed organoids developed. To evaluate CFTR activity, a FIS assay was performed. Organoids were stained with Calcein AM (Invitrogen, no. C1430) at 37°C for 30 min. Brightfield and fluorescence images (excitation/emission: 494/517 nm) were captured using a Cytation 5 plate reader (BioTek) immediately before and 4 hours after the addition of forskolin (final concentration of 10 μM). Organoid swelling at 4 hours after forskolin treatment was quantified, allowing comparison of CFTR activity between treated and untreated groups.

Patient-derived intestinal organoids treatment and Ussing chamber

This study was conducted at the Hospital for Sick Children (SickKids) in Toronto, Canada, following approved research protocol (REB no. 1000058992, SickKids Hospital, Toronto). The CFTR mutations in the patient were defined by clinical genetic testing: c.1397C>G (p.Ser466*), c.3209G>A (p.Arg1070Gln), c.1657C>T (p.Arg553*), and c.1584G>A. CF patient–derived intestinal organoids harboring complex CFTR mutations were isolated from rectal biopsies and cultured according to established culture protocols (*97*, *98*). Three-dimensional organoids growing 7 to 10 days were enzymatically dissociated using TrypLE (Thermo Fisher Scientific), suspended in growth medium (IntestiCult Human OGM, STEMCELL Technologies, no. 06010) supplemented with Y-27632, and seeded onto 2% Matrigel (Corning, no. 356231) precoated Transwell inserts (Costar 3470, 6.5 mm diameter, 0.4 μm pore size; Corning) with 100 μl medium added to the apical side and 500 μl to the basal compartment (day 0). Organoid cultures were treated with either dimethyl sulfoxide (DMSO) control, G418 (Sigma-Aldrich, no. G8168, 200 μg/ml), Trikafta, LNP–sup-tRNA, or a combination of LNP–sup-tRNA and Trikafta, with three dosages (tRNA treatment: 1.25 μg per insert). Growth media were replaced daily, and Y-27632 was removed 1 day before Ussing chamber analyses, which were performed on days 6 to 7 postseeding. Trikafta consisted of VX-445 (elexacaftor; 3 μM, Selleckchem), VX-661 (tezacaftor; 3 μM, Selleckchem), and VX-770 (ivacaftor; 3 μM, Selleckchem). VX-770 was additionally added during the Ussing chamber experiments. Electrophysiological recordings were performed using a circulating Ussing chamber system (EM-CSYS-4; Physiologic Instruments) in open-circuit mode, using symmetrical chloride-bicarbonate buffers. CFTR activity was assessed by measuring changes in transepithelial current upon addition of forskolin (Fsk, 10 μM, basolateral), designated as ΔFsk-Ieq, and verified by subsequent inhibition with CFTRinh-172 (10 μM, apical). Experiments were conducted in the presence of amiloride (100 μM) to block epithelial sodium channel activity. Data acquisition and analysis were performed using a customized LabVIEW-based software (UCP4.4.1, 2015).

Statistical analyses

Statistical analyses were performed using GraphPad Prism software (version 10.4.1). Data are presented as individual data points with means ± standard deviations (SDs), unless otherwise specified. Exact sample sizes, replicate definitions, and statistical tests are indicated in the figure legends. For cell-culture assays, biological replicates represent independently prepared cultures; multiple wells derived from the same culture preparation were treated as technical replicates and averaged before statistical analysis. For animal studies, each animal was treated as one biological replicate. For patient-derived organoid experiments, biological replicates represent independently prepared organoid-derived monolayers or measurements generated from material from a single CF participant. Comparisons between two groups were performed using two-tailed unpaired Student's *t* tests unless otherwise indicated. For comparisons among three or more groups, one-way or two-way analysis of variance (ANOVA) was used followed by post hoc multiple-comparison testing as specified in the figure legends. Dunnett's test was used when multiple treatment groups were compared with a single control, and Tukey's test was used for all pairwise comparisons. $P < 0.05$ was considered statistically significant; for sequencing and enrichment analyses, adjusted $P < 0.05$ was considered significant unless otherwise indicated. No formal sample-size or power calculation was performed before experiments; sample sizes were guided by prior studies, model feasibility, and availability of animal or patient-derived material. No formal randomization or blinding procedures were used; treatment allocation was based on genotype, sample availability, and experimental feasibility. The patient-derived organoid experiment is an n-of-1 proof-of-principle study, as it used material from a single CF study participant.

REFERENCES AND NOTES

1. J. Coller, Z. Ignatova, tRNA therapeutics for genetic diseases. *Nat. Rev. Drug Discov.* **23**, 108–125 (2024). doi: 10.1038/s41573-023-00829-9; pmid: 38049504
2. M. Mort, D. Ivanov, D. N. Cooper, N. A. Chuzhanova, A meta-analysis of nonsense mutations causing human genetic disease. *Hum. Mutat.* **29**, 1037–1047 (2008). doi: 10.1002/humu.20763; pmid: 18454449
3. R. E. Stanley, T. M. Lowe, Z. Ignatova, The regulation, function and disease relevance of cytoplasmic tRNAs. *Nat. Rev. Mol. Cell Biol.* 10.1038/s41580-026-00963-3 (2026). doi: 10.1038/s41580-026-00963-3; pmid: 42014620
4. M. Dabrowski, Z. Bukowy-Bieryllo, E. Zietkiewicz, Advances in therapeutic use of a drug-stimulated translational readthrough of premature termination codons. *Mol. Med.* **24**, 25 (2018). doi: 10.1186/s10020-018-0024-7; pmid: 30134808
5. J. Hordeaux *et al.*, Adeno-Associated Virus-Induced Dorsal Root Ganglion Pathology. *Hum. Gene Ther.* **31**, 808–818 (2020). doi: 10.1089/hum.2020.167; pmid: 32845779
6. J. R. Mendell *et al.*, Current Clinical Applications of In Vivo Gene Therapy with AAVs. *Mol. Ther.* **29**, 464–488 (2021). doi: 10.1016/j.ymthe.2020.12.007; pmid: 33309881
7. T. Anastassiadis, C. Köhrer, Ushering in the era of tRNA medicines. *J. Biol. Chem.* **299**, 105246 (2023). doi: 10.1016/j.jbc.2023.105246; pmid: 37703991
8. E. Dolgin, tRNA therapeutics burst onto startup scene. *Nat. Biotechnol.* **40**, 283–286 (2022). doi: 10.1038/s41587-022-01252-y; pmid: 35210613
9. J. C. Chang, G. F. Temple, R. F. Trecartin, Y. W. Kan, Suppression of the nonsense mutation in homozygous β^0 thalassaemia. *Nature* **281**, 602–603 (1979). doi: 10.1038/281602a0; pmid: 492326
10. G. F. Temple, A. M. Dozy, K. L. Roy, Y. W. Kan, Construction of a functional human suppressor tRNA gene: An approach to gene therapy for β-thalassaemia. *Nature* **296**, 537–540 (1982). doi: 10.1038/296537a0; pmid: 6803169
11. J. J. Porter, C. S. Heil, J. D. Lueck, Therapeutic promise of engineered nonsense suppressor tRNAs. *WIREs RNA* **12**, e1641 (2021). doi: 10.1002/wrna.1641; pmid: 33567469
12. A. Weixlbaumer *et al.*, Insights into translational termination from the structure of RF2 bound to the ribosome. *Science* **322**, 953–956 (2008). doi: 10.1126/science.1164840; pmid: 18988853
13. A. Korostelev *et al.*, Crystal structure of a translation termination complex formed with release factor RF2. *Proc. Natl. Acad. Sci. U.S.A.* **105**, 19684–19689 (2008). doi: 10.1073/pnas.0810953105; pmid: 19064930
14. J. D. Lueck *et al.*, Engineered transfer RNAs for suppression of premature termination codons. *Nat. Commun.* **10**, 822 (2019). doi: 10.1038/s41467-019-08329-4; pmid: 30778053
15. S. Albers *et al.*, Repurposing tRNAs for nonsense suppression. *Nat. Commun.* **12**, 3850 (2021). doi: 10.1038/s41467-021-24076-x; pmid: 34158503
16. W. Ko, J. J. Porter, M. T. Sipple, K. M. Edwards, J. D. Lueck, Efficient suppression of endogenous CFTR nonsense mutations using anticodon-engineered transfer RNAs. *Mol. Ther. Nucleic Acids* **28**, 685–701 (2022). doi: 10.1016/j.omtn.2022.04.033; pmid: 35664697
17. W. Ko *et al.*, ACE-tRNAs are a platform technology for suppressing nonsense mutations that cause cystic fibrosis. *Nucleic Acids Res.* **53**, gkaf675 (2025). doi: 10.1093/nar/gkaf675; pmid: 40650978
18. J. J. Porter *et al.*, Anticodon-edited transfer RNAs (ACE-tRNAs) encoded as therapeutic nonviral minimal DNA vectors. *Nucleic Acids Res.* **54**, gkag082 (2026). doi: 10.1093/nar/gkag082; pmid: 41641696
19. J. Wang *et al.*, AAV-delivered suppressor tRNA overcomes a nonsense mutation in mice. *Nature* **604**, 343–348 (2022). doi: 10.1038/s41586-022-04533-3; pmid: 35322228
20. M. Xu *et al.*, An engineered UGA suppressor tRNA gene for disease-agnostic AAV delivery. *Nat. Biotechnol.* 10.1038/s41587-025-02982-5 (2026). doi: 10.1038/s41587-025-02982-5; pmid: 41555020
21. S. Albers *et al.*, Engineered tRNAs suppress nonsense mutations in cells and in vivo. *Nature* **618**, 842–848 (2023). doi: 10.1038/s41586-023-06133-1; pmid: 37258671
22. J. M. Schrader, S. J. Chapman, O. C. Uhlenbeck, Tuning the affinity of aminoacyl-tRNA to elongation factor Tu for optimal decoding. *Proc. Natl. Acad. Sci. U.S.A.* **108**, 5215–5220 (2011). doi: 10.1073/pnas.1102128108; pmid: 21402928
23. O. C. Uhlenbeck, J. M. Schrader, Evolutionary tuning impacts the design of bacterial tRNAs for the incorporation of unnatural amino acids by ribosomes. *Curr. Opin. Chem. Biol.* **46**, 138–145 (2018). doi: 10.1016/j.cbpa.2018.07.016; pmid: 30059836
24. N. Bharti *et al.*, Translation velocity determines the efficacy of engineered suppressor tRNAs on pathogenic nonsense mutations. *Nat. Commun.* **15**, 2957 (2024). doi: 10.1038/s41467-024-47258-9; pmid: 38580646
25. S. E. Pierce *et al.*, Prime editing-installed suppressor tRNAs for disease-agnostic genome editing. *Nature* **648**, 191–202 (2025). doi: 10.1038/s41586-025-09732-2; pmid: 41261131
26. J. J. Porter, W. Ko, E. G. Sorensen, J. D. Lueck, Optimization of ACE-tRNAs function in translation for suppression of nonsense mutations. *Nucleic Acids Res.* **52**, 14112–14132 (2024). doi: 10.1093/nar/gkae1112; pmid: 39673265
27. V. de Crécy-Lagard *et al.*, Matching tRNA modifications in humans to their known and predicted enzymes. *Nucleic Acids Res.* **47**, 2143–2159 (2019). doi: 10.1093/nar/gkz011; pmid: 30698754

28. T. Suzuki, The expanding world of tRNA modifications and their disease relevance. *Nat. Rev. Mol. Cell Biol.* **22**, 375–392 (2021). doi: 10.1038/s41580-021-00342-0; pmid: 33658722
29. T. Pan, Modifications and functional genomics of human transfer RNA. *Cell Res.* **28**, 395–404 (2018). doi: 10.1038/s41422-018-0013-y; pmid: 29463900
30. W. Zhang, M. Foo, A. M. Eren, T. Pan, tRNA modification dynamics from individual organisms to metaepitranscriptomics of microbiomes. *Mol. Cell* **82**, 891–906 (2022). doi: 10.1016/j.molcel.2021.12.007; pmid: 35032425
31. I. Freund *et al.*, 2′-*O*-methylation within prokaryotic and eukaryotic tRNA inhibits innate immune activation by endosomal Toll-like receptors but does not affect recognition of whole organisms. *RNA* **25**, 869–880 (2019). doi: 10.1261/rna.070243.118; pmid: 31019095
32. L. Cui *et al.*, RNA modifications: Importance in immune cell biology and related diseases. *Signal Transduct. Target. Ther.* **7**, 334 (2022). doi: 10.1038/s41392-022-01175-9; pmid: 36138023
33. T. Ohira, T. Suzuki, Transfer RNA modifications and cellular thermotolerance. *Mol. Cell* **84**, 94–106 (2024). doi: 10.1016/j.molcel.2023.11.041; pmid: 38181765
34. G. Ronzitti, D. A. Gross, F. Mingozzi, Human Immune Responses to Adeno-Associated Virus (AAV) Vectors. *Front. Immunol.* **11**, 670 (2020). doi: 10.3389/fimmu.2020.00670; pmid: 32362898
35. E. Basner-Tschakarjan, E. Bijjiga, A. T. Martino, Pre-Clinical Assessment of Immune Responses to Adeno-Associated Virus (AAV) Vectors. *Front. Immunol.* **5**, 28 (2014). doi: 10.3389/fimmu.2014.00028; pmid: 24570676
36. A. J. Barbier, A. Y. Jiang, P. Zhang, R. Wooster, D. G. Anderson, The clinical progress of mRNA vaccines and immunotherapies. *Nat. Biotechnol.* **40**, 840–854 (2022). doi: 10.1038/s41587-022-01294-2; pmid: 35534554
37. X. Hou, T. Zaks, R. Langer, Y. Dong, Lipid nanoparticles for mRNA delivery. *Nat. Rev. Mater.* **6**, 1078–1094 (2021). doi: 10.1038/s41578-021-00358-0; pmid: 34394960
38. K. A. Hajj, K. A. Whitehead, Tools for translation: Non-viral materials for therapeutic mRNA delivery. *Nat. Rev. Mater.* **2**, 17056 (2017). doi: 10.1038/natrevmats.2017.56
39. P. R. Burgel *et al.*, Elexacaftor-tezacaftor-ivacaftor in people with cystic fibrosis harbouring two *CFTR* Class I variants: Real-world data from the French compassionate programme. *EClinicalMedicine* **88**, 103476 (2025). doi: 10.1016/j.eclinm.2025.103476; pmid: 40932846
40. D. Sordyl *et al.*, MODOMICS: A database of RNA modifications and related information. 2025 update and 20th anniversary. *Nucleic Acids Res.* **54**, D219–D225 (2026). doi: 10.1093/nar/gkaf1284; pmid: 41277531
41. N. Luo *et al.*, Near-cognate tRNAs increase the efficiency and precision of pseudouridine-mediated readthrough of premature termination codons. *Nat. Biotechnol.* **43**, 114–123 (2025). doi: 10.1038/s41587-024-02165-8; pmid: 38448662
42. S. Tijaro-Bulla, S. P. Nyandwi, H. Cui, Physiological and engineered tRNA aminoacylation. *WIREs RNA* **14**, e1789 (2023). doi: 10.1002/wrna.1789; pmid: 37042417
43. X. Qin *et al.*, Cocrystal structures of glycyl-tRNA synthetase in complex with tRNA suggest multiple conformational states in glycylation. *J. Biol. Chem.* **289**, 20359–20369 (2014). doi: 10.1074/jbc.M114.557249; pmid: 24898252
44. N. Nameki, K. Tamura, H. Asahara, T. Hasegawa, Recognition of $tRNA^{Gly}$ by three widely diverged glycyl-tRNA synthetases. *J. Mol. Biol.* **268**, 640–647 (1997). doi: 10.1006/jmbi.1997.0993; pmid: 9171287
45. R. Giegé, G. Eriani, The tRNA identity landscape for aminoacylation and beyond. *Nucleic Acids Res.* **51**, 1528–1570 (2023). doi: 10.1093/nar/gkad007; pmid: 36744444
46. Y. Li *et al.*, Crystal structures and insights into precursor tRNA 5′-end processing by prokaryotic minimal protein-only RNase P. *Nat. Commun.* **13**, 2290 (2022). doi: 10.1038/s41467-022-30072-6; pmid: 35484139
47. S. Y. Yu *et al.*, A luciferase reporter mouse model to optimize *in vivo* gene editing validated by lipid nanoparticle delivery of adenine base editors. *Mol. Ther.* **31**, 1159–1166 (2023). doi: 10.1016/j.ymthe.2023.02.009; pmid: 36793209
48. X. Han *et al.*, An ionizable lipid toolbox for RNA delivery. *Nat. Commun.* **12**, 7233 (2021). doi: 10.1038/s41467-021-27493-0; pmid: 34903741
49. B. Li *et al.*, Combinatorial design of nanoparticles for pulmonary mRNA delivery and genome editing. *Nat. Biotechnol.* **41**, 1410–1415 (2023). doi: 10.1038/s41587-023-01679-x; pmid: 36997680
50. J. Chen *et al.*, Combinatorial design of ionizable lipid nanoparticles for muscle-selective mRNA delivery with minimized off-target effects. *Proc. Natl. Acad. Sci. U.S.A.* **120**, e2309472120 (2023). doi: 10.1073/pnas.2309472120; pmid: 38060560
51. Y. Xu *et al.*, AGILE platform: A deep learning powered approach to accelerate LNP development for mRNA delivery. *Nat. Commun.* **15**, 6305 (2024). doi: 10.1038/s41467-024-50619-z; pmid: 39060305
52. J. Renner *et al.*, Synthesis of Ionizable Lipids for Gene Delivery to the Lung Using an Ugi Four Component Reaction. *J. Am. Chem. Soc.* **147**, 17459–17467 (2025). doi: 10.1021/jacs.5c04123; pmid: 40338108
53. Y. Xu *et al.*, LUMI-lab: A foundation model-driven autonomous platform enabling discovery of ionizable lipid designs for mRNA delivery. *Cell* **189**, 1620–1635.e25 (2026). doi: 10.1016/j.cell.2026.01.012; pmid: 41742414
54. K. J. Kauffman *et al.*, Optimization of Lipid Nanoparticle Formulations for mRNA Delivery in Vivo with Fractional Factorial and Definitive Screening Designs. *Nano Lett.* **15**, 7300–7306 (2015). doi: 10.1021/acs.nanolett.5b02497; pmid: 26469188
55. H. H. Ly, S. Daniel, S. K. V. Soriano, Z. Kis, A. K. Blakney, Optimization of Lipid Nanoparticles for saRNA Expression and Cellular Activation Using a Design-of-Experiment Approach. *Mol. Pharm.* **19**, 1892–1905 (2022). doi: 10.1021/acs.molpharmaceut.2c00032; pmid: 35604765
56. A. Y. Jiang *et al.*, Combinatorial development of nebulized mRNA delivery formulations for the lungs. *Nat. Nanotechnol.* **19**, 364–375 (2024). doi: 10.1038/s41565-023-01548-3; pmid: 37985700
57. J. Kim *et al.*, Engineering Lipid Nanoparticles for Enhanced Intracellular Delivery of mRNA through Inhalation. *ACS Nano* **16**, 14792–14806 (2022). doi: 10.1021/acsnano.2c05647; pmid: 36038136
58. M. P. Lokugamage *et al.*, Optimization of lipid nanoparticles for the delivery of nebulized therapeutic mRNA to the lungs. *Nat. Biomed. Eng.* **5**, 1059–1068 (2021). doi: 10.1038/s41551-021-00786-x; pmid: 34616046
59. X. Bai *et al.*, Optimized inhaled LNP formulation for enhanced treatment of idiopathic pulmonary fibrosis via mRNA-mediated antibody therapy. *Nat. Commun.* **15**, 6844 (2024). doi: 10.1038/s41467-024-51056-8; pmid: 39122711
60. A. Autour *et al.*, Fluorogenic RNA Mango aptamers for imaging small non-coding RNAs in mammalian cells. *Nat. Commun.* **9**, 656 (2018). doi: 10.1038/s41467-018-02993-8; pmid: 29440634
61. A. D. Cawte, P. J. Unrau, D. S. Rueda, Live cell imaging of single RNA molecules with fluorogenic Mango II arrays. *Nat. Commun.* **11**, 1283 (2020). doi: 10.1038/s41467-020-14932-7; pmid: 32152311
62. Y. Sun *et al.*, In vivo editing of lung stem cells for durable gene correction in mice. *Science* **384**, 1196–1202 (2024). doi: 10.1126/science.adk9428; pmid: 38870301
63. S. Suzuki *et al.*, Highly Efficient Gene Editing of Cystic Fibrosis Patient-Derived Airway Basal Cells Results in Functional CFTR Correction. *Mol. Ther.* **28**, 1684–1695 (2020). doi: 10.1016/j.ymthe.2020.04.021; pmid: 32402246
64. J. R. Rock *et al.*, Basal cells as stem cells of the mouse trachea and human airway epithelium. *Proc. Natl. Acad. Sci. U.S.A.* **106**, 12771–12775 (2009). doi: 10.1073/pnas.0906850106; pmid: 19625615
65. X. Xue *et al.*, Identification of the amino acids inserted during suppression of CFTR nonsense mutations and determination of their functional consequences. *Hum. Mol. Genet.* **26**, 3116–3129 (2017). doi: 10.1093/hmg/ddx196; pmid: 28575328
66. S. Ahmadi *et al.*, Phenotypic profiling of CFTR modulators in patient-derived respiratory epithelia. *NPJ Genom. Med.* **2**, 12 (2017). doi: 10.1038/s41525-017-0015-6; pmid: 28649446
67. J. X. Jiang *et al.*, A new platform for high-throughput therapy testing on iPSC-derived lung progenitor cells from cystic fibrosis patients. *Stem Cell Reports* **16**, 2825–2837 (2021). doi: 10.1016/j.stemcr.2021.09.020; pmid: 34678210
68. C. Wu, B. Roy, F. He, K. Yan, A. Jacobson, Poly(A)-Binding Protein Regulates the Efficiency of Translation Termination. *Cell Rep.* **33**, 108399 (2020). doi: 10.1016/j.celrep.2020.108399; pmid: 33207198
69. D. R. McHugh *et al.*, A *G542X* cystic fibrosis mouse model for examining nonsense mutation directed therapies. *PLOS ONE* **13**, e0199573 (2018). doi: 10.1371/journal.pone.0199573; pmid: 29924856
70. G. Schwank *et al.*, Functional repair of CFTR by CRISPR/Cas9 in intestinal stem cell organoids of cystic fibrosis patients. *Cell Stem Cell* **13**, 653–658 (2013). doi: 10.1016/j.stem.2013.11.002; pmid: 24315439
71. J. D. Lueck, Editing tRNA Genes to Broaden Nonsense Therapeutics. *N. Engl. J. Med.* **394**, 1651–1654 (2026). doi: 10.1056/NEJMcibr2516957; pmid: 42019025
72. L. DeFrancesco, Genome editing's third act. *Nat. Biotechnol.* **44**, 331–333 (2026). doi: 10.1038/s41587-026-03058-8; pmid: 41844972
73. M. J. Landrum *et al.*, ClinVar: Improving access to variant interpretations and supporting evidence. *Nucleic Acids Res.* **46**, D1062–D1067 (2018). doi: 10.1093/nar/gkx1153; pmid: 29165669
74. U. Varshney *et al.*, *Mycobacterium tuberculosis Rv2118c* codes for a single-component homotetrameric m^1A58 tRNA methyltransferase. *Nucleic Acids Res.* **32**, 1018–1027 (2004). doi: 10.1093/nar/gkh207; pmid: 14960715
75. V. Y. Väre, E. R. Eruysal, A. Narendran, K. L. Sarachan, P. F. Agris, Chemical and Conformational Diversity of Modified Nucleosides Affects tRNA Structure and Function. *Biomolecules* **7**, 29 (2017). doi: 10.3390/biom7010029; pmid: 28300792
76. A. Biela *et al.*, The diverse structural modes of tRNA binding and recognition. *J. Biol. Chem.* **299**, 104966 (2023). doi: 10.1016/j.jbc.2023.104966; pmid: 37380076
77. M. Frye, B. T. Harada, M. Behm, C. He, RNA modifications modulate gene expression during development. *Science* **361**, 1346–1349 (2018). doi: 10.1126/science.aau1646; pmid: 30262497
78. S. Wang, D. Weissman, Y. Dong, RNA chemistry and therapeutics. *Nat. Rev. Drug Discov.* **24**, 828–851 (2025). doi: 10.1038/s41573-025-01237-x; pmid: 40659813
79. I. A. Roundtree, M. E. Evans, T. Pan, C. He, Dynamic RNA Modifications in Gene Expression Regulation. *Cell* **169**, 1187–1200 (2017). doi: 10.1016/j.cell.2017.05.045; pmid: 28622506

80. R. Alarcon, D. Köster, S. Behrmann, Z. Ignatova, ADAM-tRNA-seq: An optimized approach for demultiplexing and enhanced hierarchal mapping in direct tRNA sequencing. *Nucleic Acids Res.* **54**, gkag022 (2026). doi: 10.1093/nar/gkag022; pmid: 41574434
81. I. Barbieri, T. Kouzarides, Role of RNA modifications in cancer. *Nat. Rev. Cancer* **20**, 303–322 (2020). doi: 10.1038/s41568-020-0253-2; pmid: 32300195
82. S. Delaunay, M. Helm, M. Frye, RNA modifications in physiology and disease: Towards clinical applications. *Nat. Rev. Genet.* **25**, 104–122 (2024). doi: 10.1038/s41576-023-00645-2; pmid: 37714958
83. K. Beebe, W. Waas, Z. Druzina, M. Guo, P. Schimmel, A universal plate format for increased throughput of assays that monitor multiple aminoacyl transfer RNA synthetase activities. *Anal. Biochem.* **368**, 111–121 (2007). doi: 10.1016/j.ab.2007.05.013; pmid: 17603003
84. C. P. Watkins, W. Zhang, A. C. Wylder, C. D. Katanski, T. Pan, A multiplex platform for small RNA sequencing elucidates multifaceted tRNA stress response and translational regulation. *Nat. Commun.* **13**, 2491 (2022). doi: 10.1038/s41467-022-30261-3; pmid: 35513407
85. L. R. Frietze, T. Pan, Bioinformatics of simultaneous, quantitative measurements of full-length tRNA and tRNA fragments by MSR sequencing. *Methods Enzymol.* **711**, 312–323 (2025). doi: 10.1016/bs.mie.2024.11.009; pmid: 39952712
86. B. Langmead, S. L. Salzberg, Fast gapped-read alignment with Bowtie 2. *Nat. Methods* **9**, 357–359 (2012). doi: 10.1038/nmeth.1923; pmid: 22388286
87. H. Li *et al.*, The Sequence Alignment/Map format and SAMtools. *Bioinformatics* **25**, 2078–2079 (2009). doi: 10.1093/bioinformatics/btp352; pmid: 19505943
88. M. I. Love, W. Huber, S. Anders, Moderated estimation of fold change and dispersion for RNA-seq data with DESeq2. *Genome Biol.* **15**, 550 (2014). doi: 10.1186/s13059-014-0550-8; pmid: 25516281
89. T. M. Lowe, P. P. Chan, tRNAscan-SE On-line: Integrating search and context for analysis of transfer RNA genes. *Nucleic Acids Res.* **44**, W54–W57 (2016). doi: 10.1093/nar/gkw413; pmid: 27174935
90. P. P. Chan, T. M. Lowe, in *Gene Prediction: Methods and Protocols*, M. Kollmar, Ed., **vol. 1962** of *Methods in Molecular Biology* (Springer, 2019), pp. 1–14.
91. E. E. Bonacquisti *et al.*, Fluorogenic RNA-based biomaterials for imaging and tracking the cargo of extracellular vesicles. *J. Control. Release* **374**, 349–368 (2024). doi: 10.1016/j.jconrel.2024.07.043; pmid: 39111600
92. A. Dobin *et al.*, STAR: Ultrafast universal RNA-seq aligner. *Bioinformatics* **29**, 15–21 (2013). doi: 10.1093/bioinformatics/bts635; pmid: 23104886
93. S. X. Ge, D. Jung, R. Yao, ShinyGO: A graphical gene-set enrichment tool for animals and plants. *Bioinformatics* **36**, 2628–2629 (2020). doi: 10.1093/bioinformatics/btz931; pmid: 31882993
94. Y. Mao, L. Jia, L. Dong, X. E. Shu, S.-B. Qian, Start codon-associated ribosomal frameshifting mediates nutrient stress adaptation. *Nat. Struct. Mol. Biol.* **30**, 1816–1825 (2023). doi: 10.1038/s41594-023-01119-z; pmid: 37957305
95. M. Martin, Cutadapt removes adapter sequences from high-throughput sequencing reads. *EMBnet. J.* **17**, 10–12 (2011). doi: 10.14806/ej.17.1.200
96. L. Calviello *et al.*, Detecting actively translated open reading frames in ribosome profiling data. *Nat. Methods* **13**, 165–170 (2016). doi: 10.1038/nmeth.3688; pmid: 26657557
97. L. Birimberg-Schwartz *et al.*, Validating organoid-derived human intestinal monolayers for personalized therapy in cystic fibrosis. *Life Sci. Alliance* **6**, e202201857 (2023). doi: 10.26508/lsa.202201857; pmid: 37024122
98. D. D. Zomer-van Ommen *et al.*, Comparison of *ex vivo* and *in vitro* intestinal cystic fibrosis models to measure CFTR-dependent ion channel activity. *J. Cyst. Fibros.* **17**, 316–324 (2018). doi: 10.1016/j.jcf.2018.02.007; pmid: 29544685

ACKNOWLEDGMENTS

The authors are grateful to the participant with CF for the organoid study at the Hospital for Sick Children. We thank Z. Ignatova and S. Albers-Fomenko for project discussions and constructive input. We thank C. A. Hodges and the Cystic Fibrosis Mouse Resource Center (CFMRC) at Case Western Reserve University (CWRU) for sharing CF mouse breeders to establish our own colonies. We thank H. Valley and the Cystic Fibrosis Foundation (CFF) Therapeutics Lab for providing cells and protocols. We thank P. J. Unrau for discussions on tRNA_Aptamer design. The authors acknowledge technical support from the Centre for Pharmaceutical Oncology for flow cytometry and imaging, the Princess Margaret Cancer Centre for access to NMR and animal facilities, the Advanced Optical Microscopy Facility (AOMF) at UHN for confocal microscopy, the Donnelly Sequencing Centre, and the Centre for Applied Genomics at the Hospital for Sick Children. Computational analyses were supported by the high-performance computing cluster operated by the University of Toronto and Compute Canada. J.C. acknowledges the doctoral-level graduate award from the NanoMedicines Innovation Network (NMIN) and the PRiME Fellowship from the University of Toronto and the Hospital for Sick Children (SickKids). C.M.M. acknowledges the support from NSERC CGS-M and CGRS-D. B.Y.S. acknowledges the support from the Ontario Graduate Scholarship. Illustration figures were created with Biorender.com. **Funding:** This work is supported by a GSK Chair Professorship (B.L.); the Leslie Dan Faculty of Pharmacy Startup Fund (B.L.); the Princess Margaret Cancer Centre Operating Fund (B.L.); Connaught Fund 523859 (B.L.); Canada Research Chairs Program CRC-2022-00575 (B.L.); Canadian Institutes of Health Research PJH-185722 and PJT-195669 (B.L.); Cystic Fibrosis Canada 1188219 (B.L.); New Frontiers in Research Fund NFRFE-2023-00203 (B.L.); Natural Sciences and Engineering Research Council of Canada RGPIN-2023-05124 (B.L.); Natural Sciences and Engineering Research Council of Canada RGPIN-2023-04305 (H.C.); National Institutes of Health grant 1R01HL174773 (B.L.); CFF grants LI23G0 and LI23I0 (B.L.); Harrington Discovery Institute HDI-BOWEN-UT_GA_44994 (B.L.); and PRiME, Next Generation Precision Medicine initiative PRMHSC2026-001 (J.C.). **Author contributions:** Conceptualization: J.C., H.C., B.L.; Funding acquisition: H.C., B.L.; Investigation: J.C., M.Z., S.D., F.G., R.T., B.Y.S., Z.R.C., Z.P.Z., J.P., Y.X., S.L., C.M.M., S.T.-B.; Methodology: J.C., T.G., J.H., H.C., B.L.; Project administration: J.C., H.C., B.L.; Supervision: H.C., B.L.; Visualization: J.C., M.Z., H.C., B.L.; Writing – original draft: J.C., H.C., B.L.; Writing – review & editing: J.C., H.C., B.L. **Competing interests:** J.C., H.C., and B.L. are inventors on an invention disclosure (no. 10004798) submitted by the University of Toronto that covers compositions, methods, and uses of the engineered and/or modified sup-tRNAs. J.C., M.Z., S.D., and B.L. are inventors on an invention disclosure (no. 10004799) submitted by the University of Toronto that covers the described ionizable lipids. The authors declare no other competing interests. **Data, code, and materials availability:** RNA-seq, ribosome profiling, and tRNA-seq data are deposited in the NCBI Gene Expression Omnibus (GEO) under accession numbers GSE303837, GSE326898, and GSE326462, respectively. All other data are available in the main text or the supplementary materials. Requests for materials should be addressed to B.L.

SUPPLEMENTARY MATERIALS

science.org/doi/10.1126/science.aeb0054
Figs. S1 to S26; Tables S1 to S5; MDAR Reproducibility Checklist
Submitted 28 July 2025; resubmitted 20 April 2026; accepted 2 July 2026
10.1126/science.aeb0054

Nonviral delivery of chemically modified tRNA rescues nonsense mutations in cystic fibrosis

Jingan Chen, Muye Zhou, Songtao Dong, Fanglin Gong, Rasangi Tennakoon, Breanna Y. Seto, Ziyan Rachel Chen, Zhichang Peter Zhou, Jingyi Pan, Yue Xu, Sijin Luozhong, Colette Maya Macarios, Santiago Tijaro-Bulla, Tanja Gonska, Jim Hu, Haissi Cui, and Bowen Li

Science **393** (6814), eaeb0054. DOI: 10.1126/science.aeb0054

Editor's summary

Nonsense mutations cause many genetic diseases by inserting premature stop codons (PTCs) that prevent full-length proteins from being made. Suppressor transfer RNAs (tRNAs) can bypass these faulty stop signals, but their current therapeutic use has been limited by inefficient PTC readthrough, immunogenicity, and delivery challenges. Chen *et al*. improved suppressor tRNAs through chemical modifications that enhanced therapeutic efficacy and persistence while reducing innate immune activation (see the Perspective by Myerson and Weissman). They also developed nonviral lipid nanoparticles tailored for pulmonary tRNA delivery. In models of cystic fibrosis ranging from cells to mice to patient-derived organoids, this nonviral approach restored the missing CFTR (cystic fibrosis transmembrane conductance regulator) protein production and function. Thus, nonviral-delivered suppressor tRNAs represent a promising therapeutic platform for treating diseases caused by nonsense mutations. —Stella M. Hurtley